A Newly Discovered Late-Cretaceous East Asian Flat Slab Explains Its Unique Lithospheric Structure and Tectonics

Diandian Peng[1] [ID], Lijun Liu[1] [ID], and Yaoyi Wang[1] [ID]

[1]University of Illinois at Urbana-Champaign, Urbana, IL, USA

Abstract The existence of historical flat slabs remains debated. We evaluate past subduction since 200 Ma using global models with data assimilation. By reproducing major Mesozoic slabs whose dip angles satisfy geological constraints, the model suggests a previously unrecognized continental-scale flat slab during the Late Cretaceous beneath East Asia, a result independent of plate reconstructions, continental lithospheric thickness, convergence rate, and seafloor age. Tests show that the pre-Cretaceous subduction history, both along the western Pacific and Tethyan trenches, is the most important reason for the formation of this prominent flat Izanagi slab. Physically, continuing subduction increases the gravitational torque, which, through balancing the suction torque, progressively reduces dynamic pressure above the slab and decreases the slab dip angle. The flat Izanagi slab explains the observed East Asian lithospheric thinning that led to the formation of the North-South Gravity Lineament, tectonic inversion of sedimentary basins, uplift of the Greater Xing'an-Taihang-Xuefeng mountains and the abrupt termination of intraplate volcanism during the Late Cretaceous.

Plain Language Summary Flat subduction refers to a downgoing slab whose dip angle is smaller than 15°. Although we can observe the present-day flat slabs through seismic imaging, it is harder to detect the ancient ones. In this study, we use global geodynamic models to simulate subduction during the past 200 Ma and find that there was a flat Izanagi slab beneath East Asia during the Late Cretaceous. This previously unrecognized flat slab provides an alternative and unified explanation for multiple synchronous geological events in East Asia, including the thin lithosphere to the east of the North-South Gravity Lineament, inversion of sedimentary basins in the region, uplift of the Greater Xing'an-Taihang-Xuefeng mountains and the termination of intraplate volcanisms. We also evaluate different mechanisms for the formation of the flat Izanagi slab and find that the most important reason is the long-lasting Mesozoic subduction along the western Pacific margin.

1. Introduction

Different from normal subduction, flat slabs have small dip angles and lie nearly horizontally beneath an overriding plate. The best examples for ongoing flat subduction are those beneath South America, clearly seen in geophysical images (Gutscher et al., 2000; Hayes et al., 2012) and likely caused by subducting oceanic plateaus and nearby cratonic roots (Hu & Liu, 2016; Manea et al., 2012). However, due to sparse observational constraints, the existence and mechanisms of flat slabs during the geological past remain debated, especially in regions with a complex tectonic history. A notable example is the Late Cretaceous-early Cenozoic Farallon flat slab beneath the western North America (Liu et al., 2010; Saleeby, 2003). This phase of flat subduction is confirmed from many aspects, including the Laramide orogeny (DeCelles, 2004; Fan & Carrapa, 2014; Saleeby, 2003), the migrating magmatic arc (Coney & Reynolds, 1977; Henderson et al., 1984; L. Liu et al., 2021), the widespread Cretaceous marine inundation (Bond, 1976; Chang & Liu, 2021; Heller & Liu, 2016), and confirmation from both forward and adjoint geodynamic modeling (English et al., 2003; Liu & Currie, 2016; Liu et al., 2008). Other examples include the Mesozoic flat subduction in East Asia (Li & Li, 2007; Liu et al., 2019; Wu et al., 2019; Xu, 2001), although questions still remain on the temporal and spatial extents of these events as well as their mechanisms (L. Liu et al., 2021).

Although uncertainties exist about past flat subduction, several lines of consensus emerge from previous studies. Besides the above-mentioned upper-plate behaviors, including orogenic uplift in the hinterland (e.g., Fan & Carrapa, 2014), migration or shutoff of magmatic arcs (e.g., Henderson et al., 1984; Liu, 2015), and contemporary inland subsidence (e.g., Dávila & Lithgow-Bertelloni, 2015; Heller & Liu, 2016), another growing agreement is that flat slab subduction could efficiently deform and thin the overriding continental lithosphere (Axen

et al., 2018; Bird, 1988; L. J. Liu et al., 2021). Indeed, all or some of these characteristics have been directing the search for past events of flat subduction, especially in regions with a complex tectonic history and imperfect mantle seismic images like East Asia (Li & Li, 2007; Wu et al., 2019).

The past decades of research also presented multiple potential mechanisms for the formation of flat slabs. These can be summarized in the following four categories. (a) Fast convergence rate, especially with the trench-ward movement of a thick overriding plate (van Hunen et al., 2000). This mechanism was used to explain both the Cretaceous western U.S. Laramide slab (Coney & Reynolds, 1977; Liu & Currie, 2016) and the Cenozoic South American flat slabs (Hu et al., 2016). (b) Increased slab buoyancy, including young seafloor ages and subduction of an oceanic plateau. This is exemplified by the Laramide-type flat slabs in the Americas (Gutscher et al., 2000; Liu et al., 2010) and East Asia (Li & Li, 2007; Wu et al., 2019). (c) Hydrodynamic suction force within the mantle wedge (Stevenson & Turner, 1977), which could be enhanced by an approaching cratonic root, with an example being the central Chillean flat slab (Hu et al., 2016; Manea et al., 2012). (d) Effects due to long-lasting prior subduction, a recently proposed mechanism based mostly on observing present-day subduction properties (Hu & Gurnis, 2020) and generic numerical models (Schellart, 2020). The physics and dynamics of this last mechanism still needs more work.

Carrying the above spirit of searching and understanding unknown flat subduction events, we reproduce the past subduction history on Earth since the early Mesozoic using a high-resolution global simulation, where we consider thermal-chemical convection (e.g., Hu, Liu & Zhou, 2018) that better represent realistic subduction processes than previous models that are always regional in scale and generic in nature (e.g., Huangfu et al., 2016; Schellart, 2020; van Hunen et al., 2004). Our global subduction models are more Earth-like because they are also based on a sophisticated data-assimilation technique (Hu, Liu & Zhou, 2018; Hu et al., 2016; Liu & Stegman, 2011) such that the model inputs are consistent with recent plate reconstructions (e.g., Müller et al., 2016; Seton et al., 2012). Based on these models, we look for possible historical flat slabs. As shown later, the model properly reproduced Mesozoic past subduction along all major convergent boundaries, with the resulting slab dip angles consistent with geological constraints. Among these, both western North America and East Asia experienced a phase of continental-scale flat slab during the Late Cretaceous. The latter represents a previously unrecognized scenario of flat subduction that can explain multiple aspects of the enigmatic tectonic history of East Asia. We further demonstrate that formation of this flat slab results from a combination of multiple proposed mechanisms.

2. Methods and Model Setup

Previous geodynamic studies on flat slab subduction mostly utilized regional models with idealized initial and boundary conditions. To better understand global subduction since the early Mesozoic, especially the existence and mechanisms of flat slabs, we quantitatively reproduced subduction history during the past 200 Ma using 4D global thermal-chemical models with data assimilation (Hu, Liu & Zhou, 2018; Hu et al., 2016; Liu & Stegman, 2011). The numerical simulations are carried out with the spherical mantle code CitcomS (McNamara & Zhong, 2004; Tan et al., 2006; Zhong et al., 2008). The mantle is discretized into a high-resolution mesh with 12 spherical caps each having $257 \times 257 \times 113$ nodes in latitude × longitude × radius. The lateral resolution is ∼23 km at the surface that reduces to ∼12 km at the core-mantle boundary (CMB). In the vertical direction, an uneven mesh is used with a ∼12 km resolution near the surface, ∼26 km near the CMB, and ∼31 km in the mid-mantle.

2.1. Governing Equations

We assume an incompressible mantle that satisfies the Boussinesq approximation. The equations for the conservation of mass, momentum and energy and the advection of chemical particles are:

$$\nabla \cdot \vec{u} = 0, \tag{1}$$

$$-\nabla P + \nabla \cdot \left[\eta \left(\nabla \vec{u} + \nabla^T \vec{u} \right) \right] + \left(\rho_m \alpha \Delta T + \Delta \rho_c \right) \vec{g} = 0, \tag{2}$$

$$\frac{\partial T}{\partial t} + \vec{u} \cdot \nabla T = \kappa \nabla^2 T, \tag{3}$$

$$\frac{\partial C}{\partial t} + \vec{u} \cdot \nabla C = 0, \tag{4}$$

where $\vec{u}$ is the velocity, P is the dynamic pressure, η is the dynamic viscosity, ρ_m is the density of the ambient mantle, α is the thermal expansion coefficient, ΔT is the temperature anomaly, $\Delta \rho_c$ is the compositional density anomaly, $\vec{g}$ is the gravitational acceleration, and C is the composition. Basic model parameters are listed in Table S1.

2.2. Boundary Conditions

The base of the mantle is assumed to be free slip. The surface assimilates velocities based on recent plate reconstructions. To quantify the influence of surface boundary conditions on mantle dynamics and slab evolution, we adopted several different plate reconstruction models (Müller et al., 2016, 2019; Seton et al., 2012) into our global simulations and compared their results. We also considered another recent reconstruction (Torsvik et al., 2019) for a comprehensive comparison of the Mesozoic kinematics in the western Pacific (Figure S1).

The temperature profile for the oceanic plates follows a modified plate model (Figure S2a) with an adjusted Rayleigh number (Hu, Liu & Zhou, 2018; Liu & Stegman, 2011). This way, the temperature difference across the thermal boundary is reduced to ~700°C from ~1300°C, in order to better resolve the evolving slab dynamics while conserving energy with a finite resolution of a discretized mesh. The convection vigor in our models remains similar to that in studies with a larger temperature contrast (Ma et al., 2019; Mao & Zhong, 2018), but whose upper-mantle dynamics is compromised with either subvertical slabs or parameterized slab geometry and kinematics. The evolving seafloor age that determines oceanic plate's thermal profile is based on plate reconstructions (Müller et al., 2016, 2019; Seton et al., 2012).

The continental plates have an initial steady-state geotherm, whose structure subsequently evolves in response to subduction dynamics. The initial thickness of the continental lithosphere varies among models, for testing their effect on slab dynamics. The CMB temperature is fixed at 500°C higher than that of the ambient mantle. This is lower than that in some earlier studies (Hassan et al., 2016; Zhang & Li, 2018), but it has little effect on subduction dynamics, due to the relatively short model history and the existence of a dense compositional layer above the CMB that prohibits excessive plume formation.

2.3. Compositional Structure

We considered the effects of 13 different chemical compositions to reproduce realistic mantle dynamics, where a total number of about 1.8 billion chemical tracers are used. The continental lithosphere consists of a two-layer crust and three-layer mantle lithosphere. The average density of continental crust is about 2.8 g/cm³ with the lower crust being weaker than the upper crust, in order to minimize the effect of imposed surface kinematics on lithospheric deformation at depth. The mantle lithosphere has a chemically buoyant upper layer, a neutrally buoyant middle layer and a dense lower layer, all relative to the ambient mantle, following a recent inference from lower lithosphere delamination (Hu, Liu, Faccenda, et al., 2018). The overall buoyancy of the continental mantle lithosphere is similar to that of a purely thermal mantle lithosphere.

The oceanic plate is approximated with three different compositions: a surface layer, a basaltic crustal layer and the underlying lithospheric mantle. The top 7-km of thickness mimics the viscosity effect of a weak and lubricating plate interface near the trenches upon subduction. Further below, we define a 21-km thick (due to the limited vertical resolution) crustal layer whose total buoyancy is the same as that for a 7-km thick oceanic crust with a density of 3.0 g/cm³. When the chemically buoyant oceanic crust subducted to 120 km or deeper, its composition and density change following the basalt-to-eclogite phase transformation.

At the base of the mantle, we also define an initial 250-km thick chemical layer whose compositional density anomaly is about +2.4% (Hassan et al., 2016; Zhang & Li, 2018). This layer evolves in response to subducting slabs and its internal thermal structure, that also generates hot plumes from time to time. By solving both thermal and compositional evolution of the mantle, our models are more capable to reproduce the multiple-scale slab dynamics, especially at shallow mantle depths, compare to the pure-thermal simulations commonly used in earlier studies.

2.4. Viscosity Structure

The models incorporate a 3D viscosity structure that depends on depth, temperature and composition (Figure S2b), following

$$\eta = \eta_0 \cdot C \cdot \exp\left(\frac{E_\eta}{T + T_\eta} - \frac{E_\eta}{T_m + T_\eta} \right), \tag{5}$$

where η is the effective viscosity, η_0 is the background viscosity (Figure S2b), C is the compositional multiplier, E_η is the activation energy, T_η is the activation temperature, T is the temperature and T_m is the background temperature. The reference viscosity is 10^{21} Pa·s. The background viscosity, activation energy and activation temperature vary within four different depth ranges: 0–44 km, 44–410 km, 410–660 km, and 660–2,867 km. The background viscosity of these layers is 10^{20} Pa·s, 10^{20} Pa·s, 10^{21} Pa·s, and 3×10^{22} Pa·s, respectively. We also considered a viscosity increase at ~1,000 km from 3×10^{22} Pa·s to 5×10^{22} Pa·s according to some recent studies (Marquardt & Miyagi, 2015; Rudolph et al., 2015). The activation energy in each depth range is 25, 42, 25, and 17 KJ/mol, respectively. The corresponding activation temperature is 100°C, 100°C, 300°C, and 300°C, respectively. Additional viscosity effects come from the compositions. Relevant to the evolution of slabs is the weak layer at the top of the oceanic plate, where a compositional multiplier is applied so that this layer has a minimum viscosity of 10^{19} Pa·s near the trenches. The models achieved up to four orders of lateral viscosity variation due to the temperature variation and compositional multipliers. This lateral viscosity variation is critical for properly simulating the asymmetric subducting slabs, horizontal mantle flow and pressure (Coltice et al., 2019; Hu, Liu & Zhou, 2018; Liu & Stegman, 2011; Zhou, Hu, et al., 2018; Zhou, Liu & Hu, 2018).

3. Results

Due to the many sophisticated model features, both in composition and viscosity, these global thermal-chemical models are very expensive to achieve. For a standard case, one full simulation starting from 200 Ma takes ~300,000 core-hours to finish. On the other hand, these simulations also better present the real Earth than 2D, regional or pure-thermal global models, in that the resolved subducting slabs are strictly one-sided with sharp viscosity and density variations across the subduction zone. More importantly, the modeled slabs could readily deflect and deform in response to lateral mantle dynamics, such as pressure gradients and mantle flow. Consequently, we observe a rich history of slab evolution and morphology, ranging from normal to flat subduction, and from continuous to segmented slabs. As shown later, the reproduced subduction history largely matches those observed/inferred along major subduction zones around the globe since the early Mesozoic. Another important outcome of these models is the temporal variation of the overriding plate, especially in the case of continental lithosphere. These allow a wide-range comparison of model results with geophysical and geological data constraints.

We present a total of 12 global models, with a focus on slab evolution under different tectonic conditions. Model 1 is the reference case, which is fully analyzed in this study. This model assimilates the surface velocity and seafloor age from Müller et al. (2016), and runs from 200 Ma to the present. The initial continental lithospheric thickness is 160 km. Models 2 and 3 have the same setting as Model 1 except that the surface boundary conditions are constrained by Seton et al. (2012) and Müller et al. (2019), respectively. Models 4 and 5 are used to test the effect of the continental lithospheric thickness, which is 200 and 120 km, respectively. Models 6–8 differ from Model 1 in that: Model 6 starts from 160 Ma (to test the effect of trench migration), Model 7 has a maximum subduction rate of 12 cm/yr after 120 Ma (to test the effect of subduction rate), Model 8 has a uniform sea floor age of 50 Myr old after 120 Ma (to test the effect of seafloor age). Models 9–11 are to test the effect of duration of continuous subduction, with the starting age being 120, 100, and 80 Ma, respectively. Model 12 is designed with a CMB temperature 500°C higher than that in Model 1 and starts from 230 Ma, to evaluate the effects of CMB temperature and subduction duration.

3.1. Simulated Global Subduction Since the Middle Mesozoic

In an earlier attempt to reproduce past global subduction (Hu, Liu & Zhou, 2018), we show that the predicted present-day slab geometry and location below major subduction zones closely match those from seismic tomography.

The new model (Model 1) presented here has a further improved fit to tomography (Figures S3 and S4), especially in regions with uncertain Mesozoic plate kinematics, such as East Asia, which will be discussed in detail later. To evaluate the fitting between modeled mantle structure and seismic tomography, we compared Model 1 with both P wave tomography models including UU-P07 (Amaru, 2007), MIT-P08 (Li et al., 2008), GAP-P4 (Obayashi et al., 2013), and S wave tomography models including SEMUCB-WM1 (French & Romanowicz, 2014) and S40RTS (Ritsema et al., 2011). These tomography models differ both in date sets and inversion methods. For example, UU-P07 (Amaru, 2007) used ~18 million P wave arrivals, and 3-D ray tracing and earthquake relocation methods. MIT-P08 (Li et al., 2008) used ~15 million P wave arrivals and 3-D finite frequency kernels to integrate the long and short period data. GAP-P4 (Obayashi et al., 2013) used ~11.3 million long period P wave arrival time data and ~15,000 short period PP–P differential time data, and finite frequency kernels were calculated. SEMUCB-WM1 (French & Romanowicz, 2014) employed a hybrid waveform-inversion method for 273 seismic events. S40RTS (Ritsema et al., 2011) used data of 20 million Rayleigh wave phase velocity measurements, 500,000 teleseismic body-wave travel times and 84,000 normal-mode splitting functions.

To evaluate the model results, we compared Model 1 results with tomography models in two different ways. The first way is through qualitative cross-section comparison, where we evaluate the temperature predicted in Model 1 against P wave tomography models (e.g., Figure S3), which have better resolution for slabs near subduction zones than S wave tomography models in general. Beneath all major subduction zones including East Asia, South Asia, North America, and South America, the slabs in Model 1 are generally consistent with P wave tomography UU-P07 (Figure S3). To further quantify the fitting to tomography, we apply a second approach (see Method in SI for details), which analyzes the model results in the spherical hormonic domain following the method in multiple previous studies (Becker & Boschi, 2002; Mao & Zhong, 2019). The overall correlation for spherical harmonic degrees 1–20 (Figure S4) are improved from previous studies (e.g., Mao & Zhong, 2019). For example, the weighted total correlation with SEMUCB-WM1 is $<r_8> = 0.52$ ($<r_{20}> = 0.37$) for degrees 1–8 (1–20) in a depth range of 50–2,815 km. When the depth is limited to lower mantle, the total correlations are $<r_8> = 0.55$ and $<r_{20}> = 0.37$. The total correlation of Model 1 with S40RTS is better, with weighted total correlations of $<r_8> = 0.53$ and $<r_{20}> = 0.39$ in a depth range of 50–2,815 km, and $<r_8> = 0.56$ and $<r_{20}> = 0.38$ in the lower mantle. The increased values of total correlations from previous studies (e.g., Mao & Zhong, 2019) support the improved model results in this study. Consequently, the fit to the present mantle structures lends credibility to the simulated past subduction (Figure 1).

Since 200 Ma, subduction along the four major trenches (North America, South America, East Asia, and South Asia) has fluctuations of slab dip angle resulting in steep to shallow dipping subduction. The predicted slabs along the South American and Tethyan trenches during the Mesozoic are predominantly normal with a >30° dip angle in general (Figure S3). These are consistent with paleo-positions of magmatic arcs along Tethyan (Kapp & Decelles, 2019) and South American trenches (Trumbull et al., 2006), suggesting that their slab dip angels have been mostly normal throughout the Mesozoic. The model also predicted a brief Late-Cretaceous flat slab within South Asia (Figure 1) and a flat Nazca slab beneath South America at the present day (Figure S3), both of which also match observation (Hu et al., 2016; X. Zhang et al., 2019).

During the entire model history, we observe the occurrence of two prominent (extending no less than 1,000 km inland) flat slabs, both at a continental scale (>1,000 km wide along trench), long-lasting (for 40–50 Myr), and occurring in the Late Cretaceous to Early Cenozoic. One is the well-studied Farallon flat slab from 90 to 40 Ma within the western North America (Figures 1 and S3). The modeled flat Farallon slab reached an inland distance of ~1,000 km at the maximum, consistent with but slightly shorter than inferences from structural deformation (Saleeby, 2003) and that in time-reversed convection models based on tomography images (Liu et al., 2008, 2010). Formation of the flat Farallon slab has been commonly attributed to the fast motion of the overriding plate (e.g., Liu & Currie, 2016; van Hunen et al., 2000). Consideration of a buoyant oceanic plateau (Liu et al., 2010), a process not modeled here, may further increase the width of the flat slab. The reproduction of the Farallon flat slab in Model 1 confirms its improved capability for resolving past subduction over similar previous studies (e.g., Ma et al., 2019; Mao & Zhong, 2018).

The other prominent flat slab occurred within the western Pacific, where the subducting Izanagi slab broadly underplated East Asia during the Late Cretaceous (100–60 Ma). The landward extent (up to 1,600 km) of the flat Izanagi slab was even larger than that of the flat Farallon slab (Figure 1). This flat slab was neither previously recognized nor reproduced in any earlier geodynamic models. An important way to constrain abnormal past
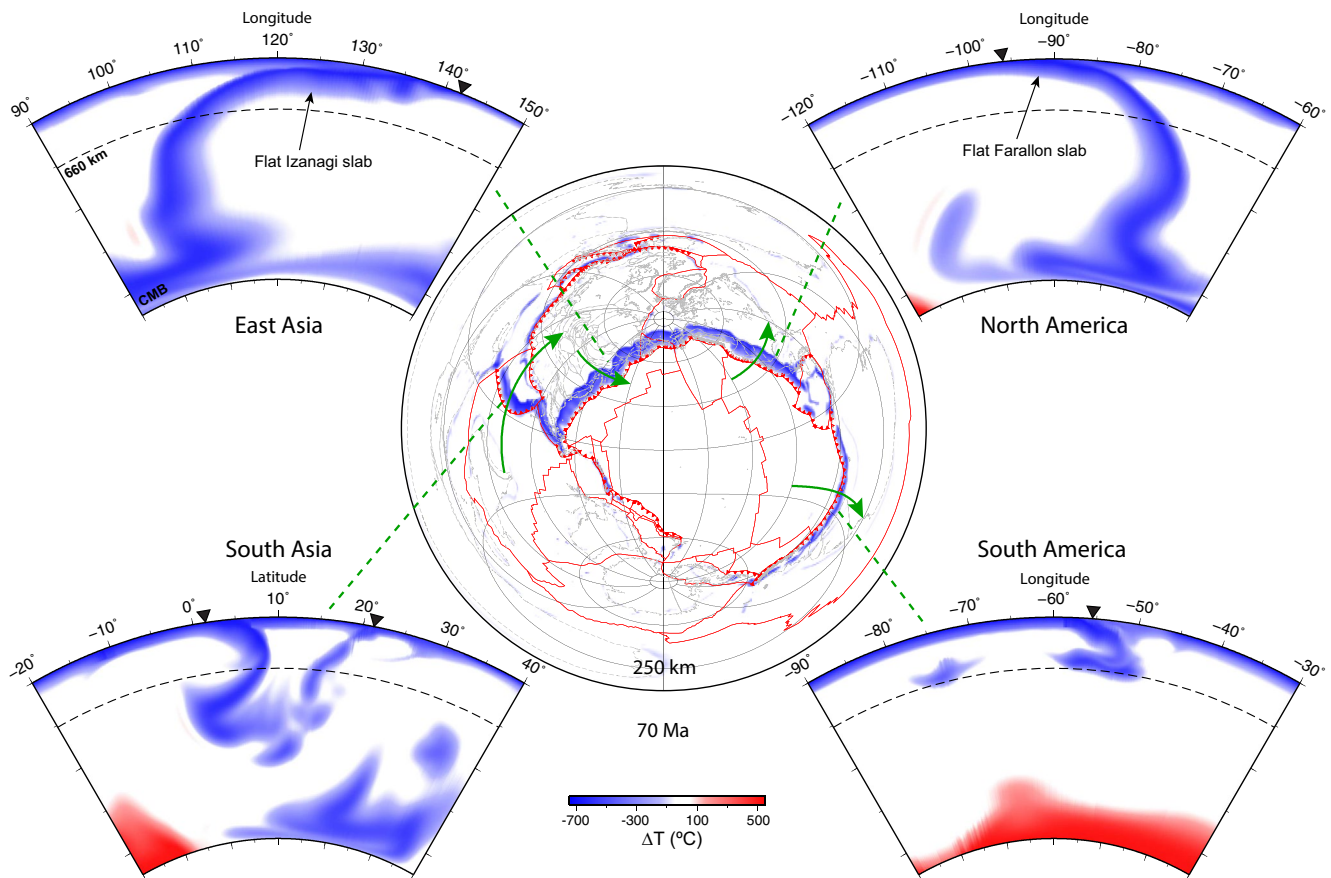
Figure 1. A global view of subducting slabs at 70 Ma from Model 1. The map in the center shows temperature at 250 km. The positions of the cross-sections are marked on the map as green arrowed lines. The arrows on the map show the left-to-right direction of the cross-sections. Along these major subduction zones, East Asia and North America had flat subduction during the Late Cretaceous, while the Tethyan and South American slabs did not.

subduction behaviors is to compare with the present-day mantle structure (Hu, Liu & Zhou, 2018; Liu & Stegman, 2011). Figure 2 shows this comparison with seismic tomography models MIT-P08, GAP-P4, and UU-P07. The Mesozoic slabs are predominantly within the lower mantle at the present, where both predicted geometry and location of the lower-mantle slabs match those revealed in tomography, providing an additional support for the modeled Mesozoic subduction within the western Pacific.

Another inference of Late-Mesozoic flat subduction directly comes from the seismic image itself. The majority of the lower mantle slab, as well as the top of it (~1,000 km), is located far west to the present-day trench, with a distance of up to 3,000 km (Figures 2c–2h). However, the Eurasian Plate has experienced limited eastward translation (<1,000 km) since the Mesozoic (Figure S1), as demonstrated in several recent plate reconstructions (Müller et al., 2016, 2019; Seton et al., 2012; Torsvik et al., 2019). This large east-west offset between the Mesozoic slab and present-day trench location suggests a significant horizontal displacement of the slab since it entered the mantle. This displacement could be due to trench retreat, lateral slab migration in the mantle, or a past flat slab. Based on the reproduced evolution of major slabs (Figure S3) and given the limited amount of trench retreat (Figure S2), we suggest a broad Mesozoic flat slab provides the most plausible explanation for the present-day seismic image. This reasoning is effectively the same as the inference of the flat Farallon slab during the Late Cretaceous (Figures 1 and S3) based on geodynamic modeling using seismic images (Bunge & Grand, 2000; Liu et al., 2008).

Since there are considerable amounts of uncertainty in the Mesozoic plate motion (Figure S1), we further tested models (Model 2 and Model 3) constrained by two other plate reconstructions (Müller et al., 2019; Seton et al., 2012). These reconstructions show quite different histories of west Pacific subduction and East Asian motion from that use in Model 1 (Figure S1). Although the resulting Late-Cretaceous slab geometries from Models
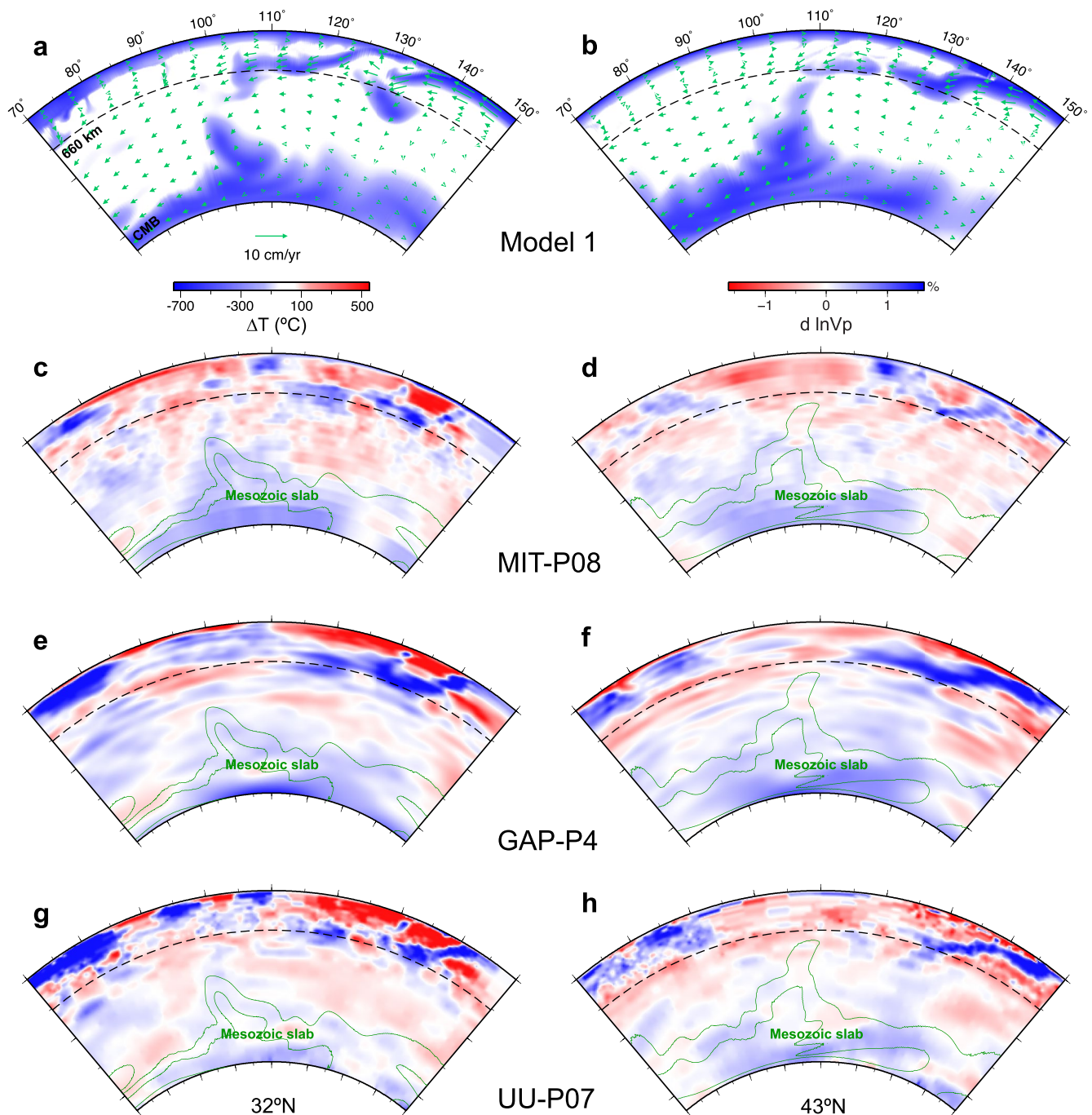
Figure 2. Model results versus tomographic image for the present mantle structure. (a and b) Model predicted slab geometry and mantle flow at the present day along 32°N and 43°N, respectively. (c and d) P wave anomalies from the tomography MIT-P08 along 32°N and 43°N, respectively. Panels (e and f) the same as panels (c and d) but for GAP-P4. Panels (g and h) the same as panels (c and d) but for UU-P07. The modeled lower-mantle slabs are mostly due to Mesozoic subduction, and are highlighted using green contours showing two different isotherms at 100°C and 400°C colder than the ambient mantle. Note that the location and geometry of modeled slabs are consistent with those of the seismic image.

2 and 3 are not identical to that in Model 1, both these models also clearly demonstrate a flat Izanagi slab (Figure S5) whose location and timing are largely consistent with that in the reference case. Thus, we conclude that the Late-Cretaceous East Asian flat slab represents a robust model result that is independent of surface kinematic conditions.
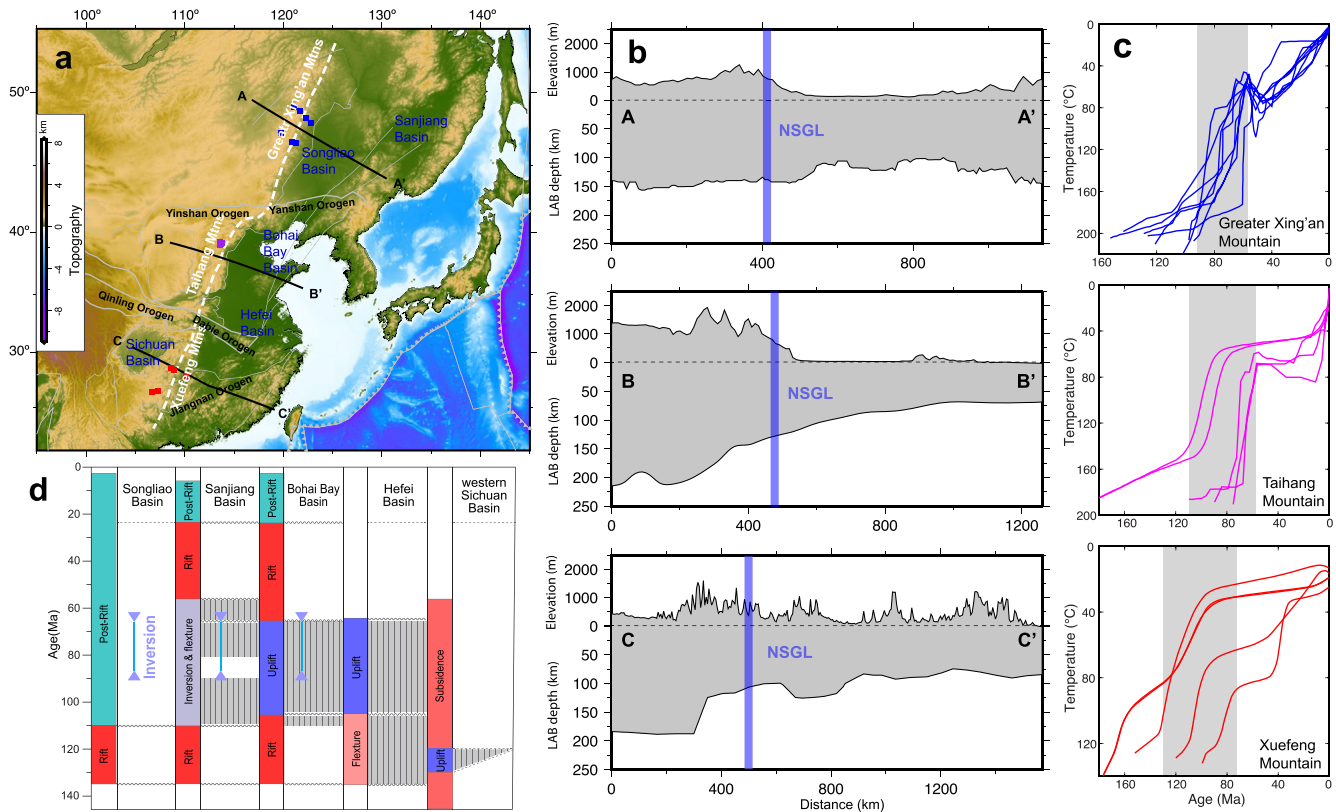
Figure 3. Geological constraints for the flat Izanagi subduction during the Late Cretaceous. (a) Topography of East Asia. The NSGL (white dashed curve), which extends from Northeast China to South China, cuts the east-west trending tectonic belts including the Yinshan-Yanshan Orogen, Qinling-Dabie Orogen, and Jiangnan Orogen. (b) The elevation and lithosphere-asthenosphere boundary (LAB) depth along AA', BB', and CC' (based on Zhang et al., 2014, 2018; Y. Zhang et al., 2019), positions are marked in panel (a). To the eastern side of the NSGL, the elevation is lower, and LAB is shallower. (c) Thermochronology models for Greater Xing'an-Taihang-Xuefeng mountains (based on Clinkscales et al., 2020; Ge et al., 2016; Pang et al., 2020; Qing et al., 2008). The samples are marked in panel (a) by squares with colors corresponding to the colors of the curves. The shaded zones show the time periods with major cooling events. At different locations, the time is consistent. (d) The sedimentary history of Songliao Basin, Sanjiang Basin, Bohai Bay Basin, Hefei Basin, and western Sichuan Basin (based on Li et al., 2016; Liu et al., 2017, 2020). The gray column bars show the stratum loss. The period of basin inversion is marked by the purple line.

3.2. Geological Constraints on a Potential Late-Cretaceous Flat Izanagi Slab

Here we further evaluate the predicted Late-Cretaceous flat Izanagi slab following the common exercises on constraining the flat Farallon slab (Axen et al., 2018; Liu et al., 2010; Saleeby, 2003). We first emphasize that, due to the poorly known Mesozoic subduction history in the western Pacific, our model result represents a previously unrecognized episode of flat slab that could have significantly affected the tectonics of the region. However, before a final conclusion is achieved, multiple additional aspects of the model and surface geology need to be examined, similar to that done for the Farallon flat slab mentioned above.

Here, we focus on evaluating the flat Izanagi subduction with several unique aspects of the Mesozoic tectonic history of East Asia, including the enigmatic formation of the North-South Gravity Lineament (NSGL), the abrupt inversion of major sedimentary basins east of the NSGL, the synchronous exhumation of the NSGL-parallel Greater Xing'an-Taihang-Xuefeng mountains, and enhanced Late-Cretaceous subsidence within the Sichuan basin further west (Figure 3). Refer to a detailed review of the region's Mesozoic tectonic history and possible links to past flat subduction events (L. J. Liu et al., 2021).

First, the NSGL highlights strong east-west contrasts in topography (Figure 3a), Bouguer gravity anomaly (Xu, 2007), crustal thickness (Li et al., 2014), and lithospheric thickness (Figure 3b). It cuts through major east-west trending Early-Mesozoic tectonic belts (Yinshan-Yanshan Orogen, Qinling-Dabie Orogen, and Jiangnan Orogen) in East Asia (Figure 3a). This implies that the appearance of the NSGL is likely after the formation of these east-west tectonic belts. This provides a first-order age constraint for the formation of the NSGL to
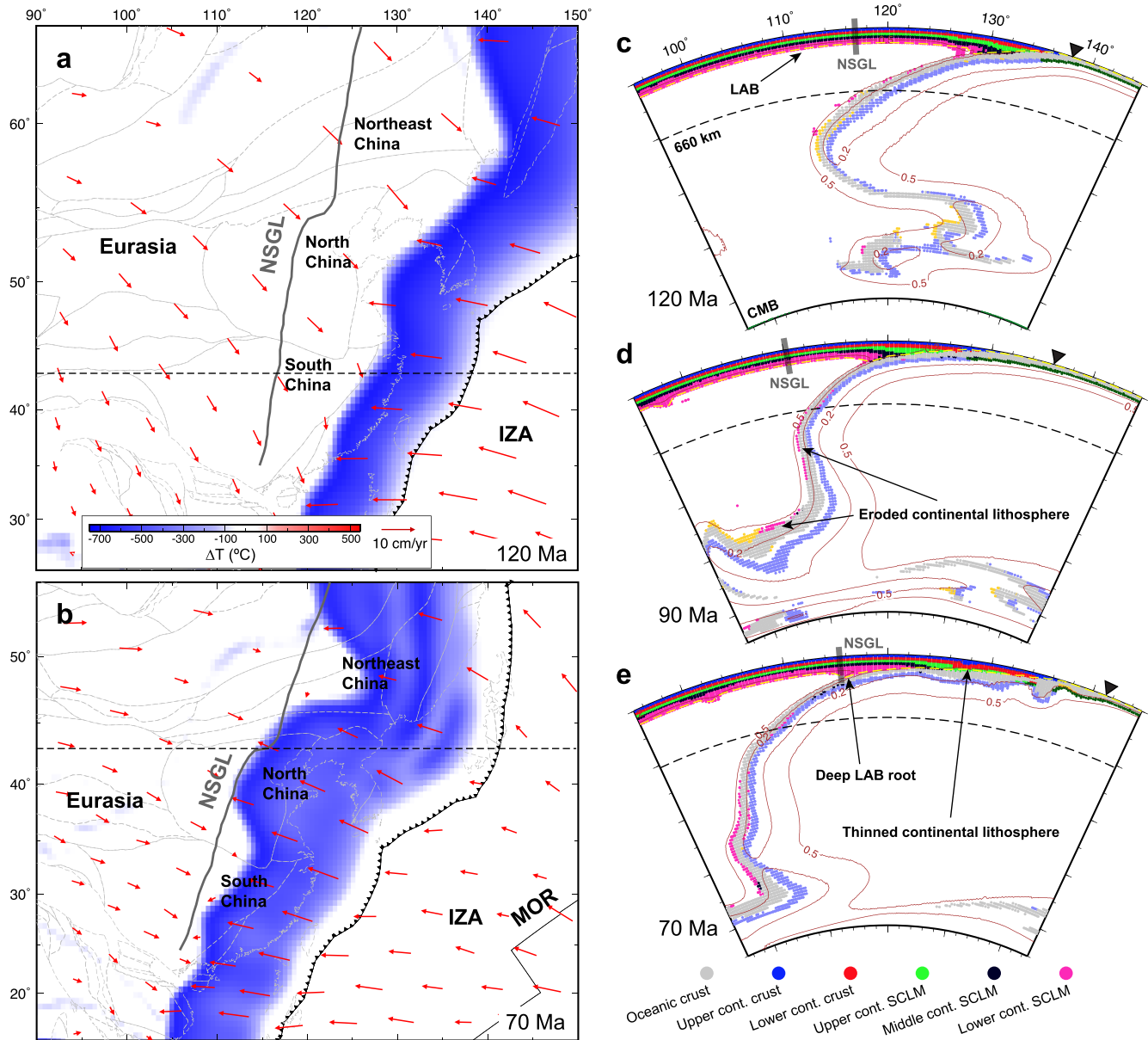
Figure 4. Evolution of the Izanagi slab and mantle flow in Model 1. (a and b) Map view at the depth of 250 km at 120 and 70 Ma, respectively. The background temperature represents mantle temperature anomaly. Arrows represent mantle flow. The gray dashed lines show the locations of North-South Gravity Lineament (NSGL) that are restored to the past following a plate reconstruction model (Müller et al., 2016). (c–e) Cross-sectional view of the compositional field along 43°N at 120, 90, and 70 Ma, respectively. The contours show nondimensional temperatures of 0.2 and 0.5. Black triangles in panels (c–e) mark the trench locations. The gray bars show the NSGL locations.

be no earlier than the Early Mesozoic (Xu, 2007). Previous studies show that a flat slab can result in thinning of the overriding continental lithosphere, with the amount of thinning depending on the model setup (Axen et al., 2018; Bird, 1988). Multiple conceptual models of East Asian flat subduction were proposed (Li & Li, 2007; Liu et al., 2019; Wu et al., 2019; Zhang et al., 2010), but they all imply more restricted spatial extents and at earlier times relative to those of the NSGL.

In contrast, the flat Izanagi slab in our model underplated the entire N-S range of East Asia (Figure 4). During its development, the western edge of the flat slab advanced westward until it reached the location of the NSGL by 70 Ma when the flat slab reached the maximum inland extent (Figure 4). This flat slab had an east-west length of ~1,600 km in South China (e.g., 32°N) and of ~1,800 km in North China (e.g., 43°N). With the development

of the flat slab, the overriding Eurasian mantle lithosphere was eroded by the slab (Figures 4c–4e), leading to a much-reduced lithospheric thickness to the east of the NSGL. In addition, some eroded and displaced continental lithospheric material accumulated at the western end of the flat slab to form a deep root. This lithospheric root is also consistent with several seismic studies (Chen et al., 2014; Liu et al., 2004; Sun & Kennett, 2017). These observations suggest that lithosphere thinning due to the newly revealed flat slab is a plausible mechanism for the formation of the NSGL.

During flat slab subduction, the overriding plate tends to experience lithospheric compression, as seen in the typical Laramide Orogeny (DeCelles, 2004; Liu et al., 2010). In East Asia, almost all major sedimentary basins to the east of the NSGL (e.g., Songliao Basin, Sanjiang Basin, Bohai Bay Basin, and Hefei Basin in Figure 3d) experienced a ~30-Myr period of inversion during the Late Cretaceous (Liu et al., 2017, 2020). The origin of this continental-scale basin inversion remains elusive. Previous proposals include changing plate motion and/or trench advance around this time (Liu et al., 2017; Song et al., 2014), but they are not supported by recent plate reconstructions (e.g., Figure S1). Our model, on the other hand, suggests that the flat slab provides a direct mechanism for this event. Indeed, the transition from extensional/strike-slip type of stress at 120 Ma (Figure S6a) to strong east-west compressional stress at 70 Ma (Figure S6b) within East Asia is consistent with the change from rapid Early-Cretaceous rift-basin deposition to regional-scale Late-Cretaceous basin inversion. During this process, the flat subduction induced compression thickened the buoyant upper mantle lithosphere (Figures 4c and 4d), and could have likely thickened the crust as well, where the latter was not simulated in our model due to imposed surface kinematics. Consequently, the resulting surface uplift caused the basin inversion east of the NSGL where the crust was weaker than on the west. Meanwhile, the sedimentary records of the Sichuan Basin (west of the NSGL, Figure 3d) reveals subsidence during most of the Cretaceous, with the subsidence rate increased from 10 m/My during 125–90 Ma to 30 m/My during 90–66 Ma (Li et al., 2016), where the enhanced subsidence rate closely tracks the timing of slab flattening during the Late Cretaceous (Figures 4 and 6). This pattern of surface uplift above the flat slab and subsidence at the leading slab edge is consistent with previous studies for the South American flat subduction (Dávila & Lithgow-Bertelloni, 2015; Flament et al., 2015).

Another important indication for surface uplift is orogenic exhumation (e.g., Fan & Carrapa, 2014). While the timing for the formation of the NSGL is constrained to be Late Mesozoic, Xu (2007) further used the time of the Taihang Mountain uplift to suggest that the NSGL formed in Early Cretaceous. In this study we revisited the cooling history of the Greater Xing'an-Taihang-Xuefeng mountain chain that goes along the NSGL. According to recent thermochronology studies (Clinkscales et al., 2020; Ge et al., 2016; Pang et al., 2020; Qing et al., 2008), all the mountains along the NSGL lineament experienced rapid cooling during the Late Cretaceous (Figure 3c). These cooling events were previously attributed to different mechanisms, including orogenic uplifts (Ge et al., 2016; Pang et al., 2020; Qing et al., 2008) and extension (Clinkscales et al., 2020). Given that both the timing and spatial distribution of the flat slab in our model (Figure 4) match those of the basin inversion and orogenic exhumation (Figure 1), we suggest that the regional compression and uplift due to flat subduction provides an alternative mechanism to these surface records. Formation of the deep lithospheric roots right below the Greater Xing'an-Taihang-Xuefeng mountains (Figure 4e) also seems to suggest a causal relationship.

Based on the strong consistency between the modeled flat Izanagi slab and various tectonic observations, we suggest that uplift of the Greater Xing'an-Taihang-Xuefeng mountains and thinning of the lithosphere to the east characterize the formation of the NSGL during the Late Cretaceous.

3.3. Evaluating Proposed Mechanisms for Slab Flattening

While a Late-Cretaceous flat Izanagi slab was consistently produced in models assimilating constraints from different plate reconstructions, the mechanism for the observed slab flattening still remains to be investigated. Here we will evaluate all previously proposed mechanisms including (a) enhanced hydrodynamic suction; (b) large convergence rate; (c) increased slab buoyancy; and (d) long-existing prior subduction. The first mechanism mainly concerns the effect of a thick cratonic overriding plate that helps to increase the suction force and to reduce the slab dip (Hu et al., 2016; Jones, 2012; Liu & Currie, 2016; Manea et al., 2012). In Model 1, all continents have the same initial thickness (160 km), with no thick cratonic roots included. As shown above (Figures 4 and S3), flat subduction in East Asia did not appear within the first 100-Myr of model time, and the Late-Cretaceous slab flattening was not assisted by any nearby thick craton. In addition, North China Craton, the closest craton to the inferred flat Izanagi slab, is narrow with less than half the width of the flat slab in our models. Therefore, a thick
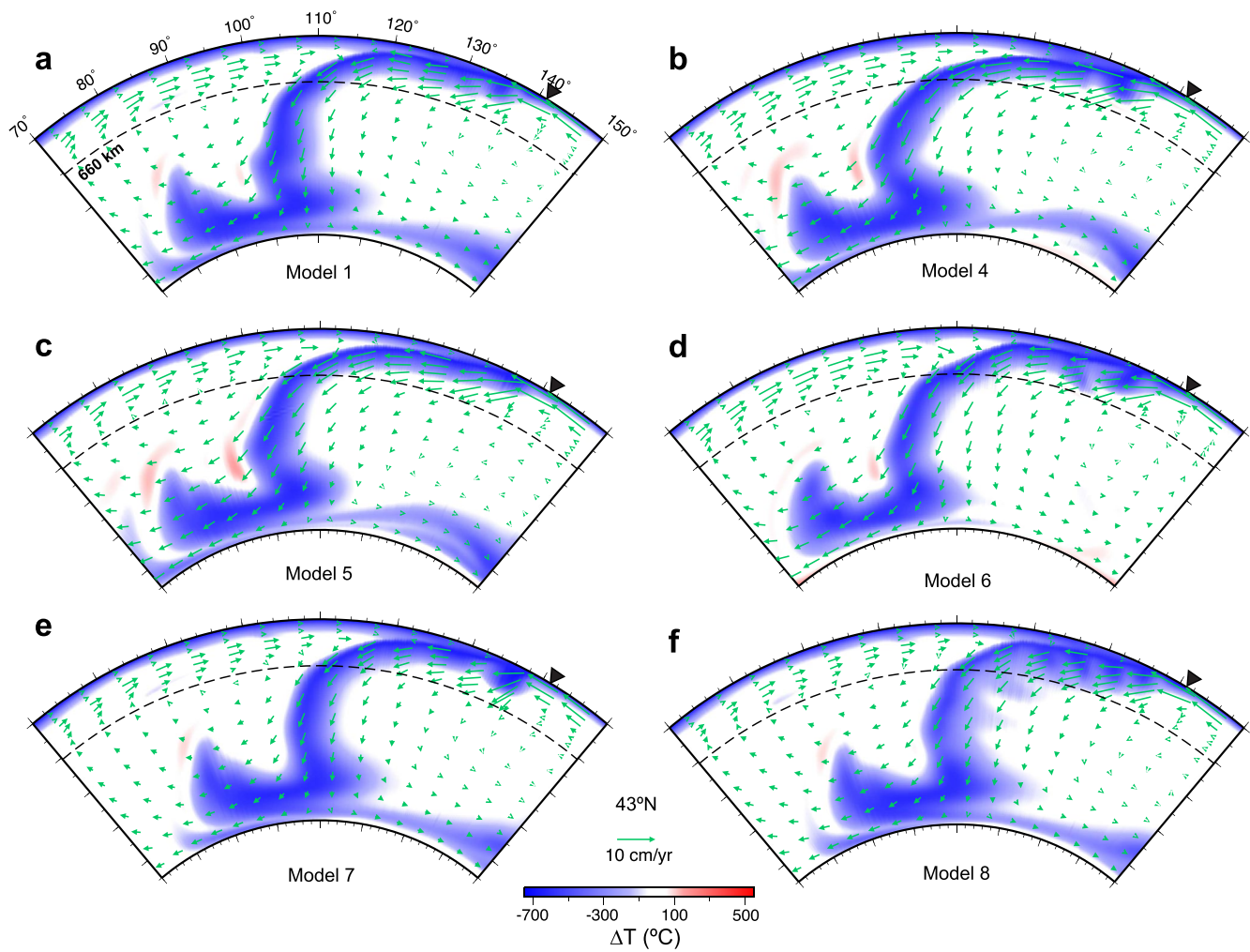
Figure 5. Slab geometries along 43°N at 70 Ma in different models. Black triangles show trench locations. Note that all these models have the flat Izanagi slab.

overriding cratonic plate is not required for the flat Izanagi slab to form. We further run Model 4 and Model 5, with overriding plate lithospheric thickness being 200 and 120 km, respectively. The observation that both these two models result in a similar flat Izanagi slab confirms that the lithospheric thickness of the overriding plate is not important for the formation of flat subduction (Figures 5a–5c).

The convergence rate is the sum of the overriding plate motion (equal to trench migration rate if neglecting intraplate deformation) and subducting plate motion. To test the potential effect of trench motion prior to the formation of the flat slab, we performed another model (Model 6), which started from 160 Ma instead of 200 Ma. Since the net trench migration during 160–60 Ma is very small (<10° arc length, Figure S1), this model also represents a scenario where the long-term trench effect is negligible. Surprisingly, Model 6 also generated a flat Izanagi slab (Figure 5d) with almost identical geometry to that in Model 1 (Figure 5a). Based on these model results (Figures 5a and 5d), we suggest that trench migration is not the most important reason for the formation of the Late-Cretaceous flat Izanagi slab.

Another key component of the convergence rate is the speed of the subducting plate. Recent plate reconstructions suggest that the subduction speed of the Izanagi plate increased significantly during the Late Cretaceous (Müller et al., 2016, 2019; Seton et al., 2012). According to Müller et al. (2016), the average Izanagi plate velocity during 120–100 Ma is about 12 cm/yr (Figure S7). After that the Izanagi plate sped up, with the velocity going up to 23 cm/yr by 80 Ma. The fast subduction speed was also proposed as a possible reason for the Late-Cretaceous flat subduction of the Farallon plate (Coney & Reynolds, 1977). Since the modeled slab became flattened after ~100 Ma (Figure S3), which corresponds to the time of Izanagi speeding up (Figure S7), we performed another

model (Model 7), in which the upper limit of the subduction speed is capped at 12 cm/yr after 120 Ma but other model setup remains the same as that in the reference model. However, we observe that without the period of fast Izanagi plate motion, the flat Izanagi slab still came into being during the Late Cretaceous, where the resulting slab geometry (Figure 5e) is almost identical to that in the reference case (Figure 5a). This additional model result suggests that the fast subduction speed is not causing the predicted flat slab. Collectively, the results from these cross-sections (Figures 5a, 5d and 5e) imply that the convergence rate is not the reason for the formation of the flat Izanagi subduction.

Increased slab buoyancy force is another popular mechanism to explain the origin of flat subduction (Liu et al., 2010; van Hunen et al., 2002). Common approaches for increasing slab buoyancy include the presence of oceanic plateaus within the ambient seafloor and the presence of young seafloor age. In our models, the thermal structure of the oceanic lithosphere follows the plate model, where the lithospheric thickness varies when seafloor age is less than 80 Myr. However, no oceanic plateau is included within the Izanagi plate for any time during the simulation. This proves that an oceanic plateau is not required for the occurrence of the flat subduction. Regarding the effect of young seafloor age, a consensus-based on multiple plate reconstructions (Müller et al., 2016, 2019; Seton et al., 2012) is that the Izanagi plate became younger at the trench during the Late Cretaceous, prior to the Izanagi-Pacific mid-ocean ridge entering the subduction zone at around 55 Ma. Thus, the slab age could be as young as 10 Ma during the latest Cretaceous. Since the average seafloor age of the Izanagi Plate during the Late Cretaceous is about 50 Myr, we designed a new model (Model 8) whose seafloor age remained as 50 Myr-old after 120 Ma. Model eight is otherwise the same as the reference model. Interestingly, this model still reproduced the Late-Cretaceous flat slab (Figure 5f). Although minor differences in slab thickness and geometry exist in this simulation, the length of the resulting flat slab is very similar to that in Model 1 (Figure 5a). Based on these results, we conclude that the slab age is not a dominant control on the generation of the flat Izanagi slab as well.

3.4. The Role of Former Subducted Slabs

Active subduction will generate low (high) dynamic pressure above (below) the slab (Stevenson & Turner, 1977). The resulting pressure-gradient across the slab, also called hydrodynamic suction, is balanced by the negative buoyancy of the slab to maintain a certain dip angle. Consequently, a larger pressure-gradient results in a smaller slab dip (Stevenson & Turner, 1977). This dynamic relationship is commonly observed in our model. Take Model 1 for an example (Figure 6), at 160 Ma (40 Myr after subduction initiated), the dynamic pressure in the mantle wedge was only slightly lower than that below the slab hinge, as correlated with a relative steep Izanagi slab (Figure 6a). By 120 Ma (80 Myr of continuous subduction), the low pressure within the mantle wedge became more prominent, and meanwhile the slab dip was also notably reduced (Figure 6b). This trend progressed further into the Late Cretaceous, during which the slab became progressively flatter while the dynamic pressure above the slab continued to decrease (Figures 6c and 6d). A similar evolution history of dynamic pressure and slab dip also occurred along the Tethyan subduction zone in South Asia (Figures 6 and S3).

While the above corner-flow analysis explains the instantaneous force balance of an evolving subducting slab, it remains unclear what drives the progressive pressure reduction above the slab and the reduction in slab dip during the late Mesozoic. With more tests, we found that the duration of continuous prior subduction along the same trench is the key reason for the observed slab flattening. To illustrate this causal relationship, we compared the model results (i.e., dynamic pressure and slab geometry) at 70 Ma from four models that have different starting ages of subduction (Figure 7): 200 Ma (Model 1), 160 Ma (Model 6), 120 Ma (Model 9), 100 Ma (Model 10), and 80 Ma (Model 11), respectively. Overall, with an earlier starting age, the resulting Late-Cretaceous slab dip is smaller (Figures 7, S8, and S9). When subduction started at 80 Ma, the slab by 70 Ma was steeply subducting and barely reached the base of the upper mantle (Figures 7e and S8e). As the starting age increases to 100 Ma, the slab at 70 Ma was more shallowly dipping but not flattened, with its lower end entering the lower mantle (Figures 7d and S8d). An upper-mantle flat-slab started to form at 70 Ma as we push the starting age back to 120 Ma (Figures 7c and S8c). In this case (Model 9), the length of the flat slab is notably smaller than that in Model 1 (Figure 7a). This relationship is further confirmed with Model 6 whose subduction started at 160 Ma (Figure 7b), where the length of the 70-Ma flat slab is almost identical to that in Model 1 (Figure 7a). Another way to understand the above statement is through analyzing the mean slab dip angle at different depth ranges (Figure 7f). The shallow portions of the slab (0–300 km) demonstrate a clear trend with the dip angle decreasing as the subduction
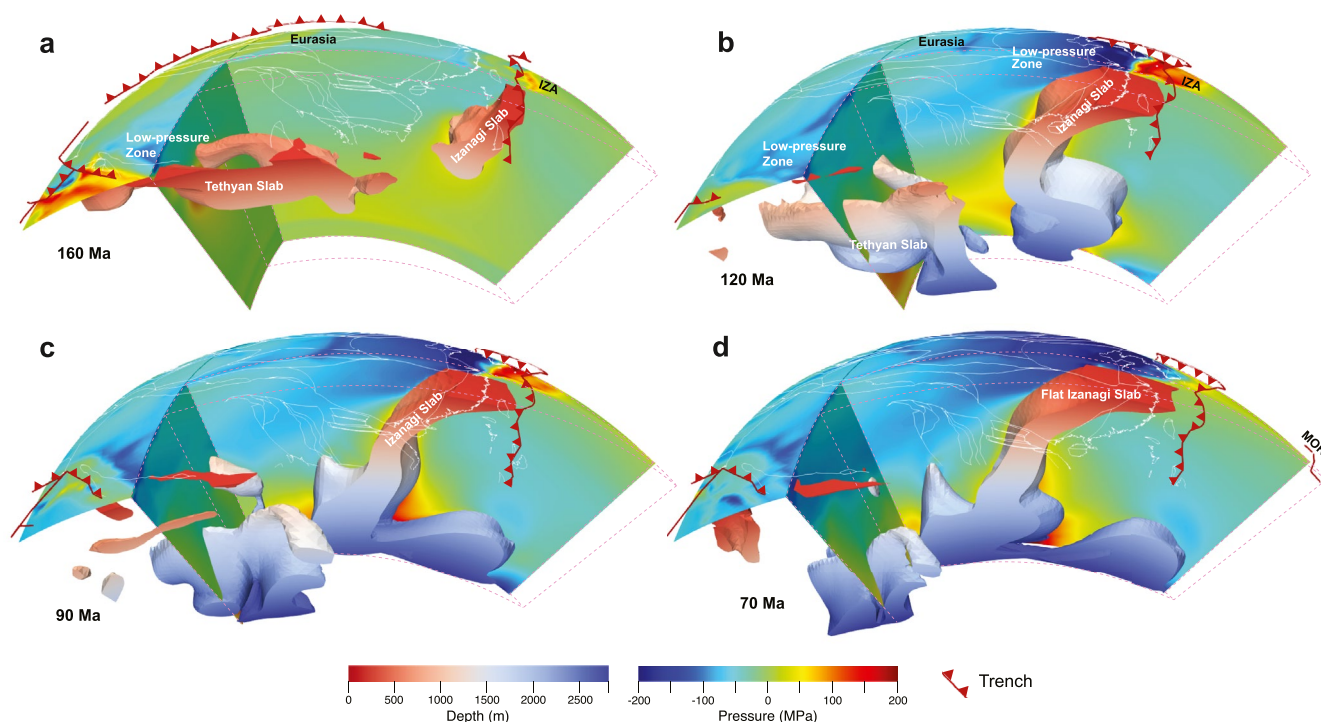
Figure 6. 3D view of the evolving dynamic pressure and slab geometry in Model 1. Slabs are shown as isovolumes with a non-dimensional temperature lower than 0.45, where the color of the slab represents depth, from 200 km to the core-mantle boundary. On the spherical surface (at 100 km depth) and the vertical cross sections, color represents dynamic pressure. White curves show coastlines and tectonic provinces, while red curves show plate boundaries. Orange dash grid lines mark the position of several cross-sections that cut the Izanagi slab and dynamic pressure field.

duration increases. This finding suggests that the deep mantle dynamics associated with different subduction durations strongly controls the slab dip above 300 km depth, where the resulting dynamic pressure plays a dominant role. The actively descending slabs, regardless of their depths, are affecting the upper mantle dynamic pressure distribution and thus the slab dip at shallow depth. According to Wu et al. (2019), the Late-Jurassic flat slab below North China started to steepen after 160 Ma, a process not modeled here. The fact that Model 1 and 6 have similar results (Figures 7a, 7b, S9a and S9b) demonstrates that subduction prior to 160 Ma has little effect on the formation of the 70-Ma flat slab. Model 12 which starts from 230 Ma also has a similar flat Izanagi slab as in Model 1 (Figure S10), and thus further supports the above statement. Therefore, the Late-Cretaceous flat slab represents an independent result from subduction prior to the Cretaceous.

Importantly, these models reveal that the dynamic pressure above the 70-Ma slab became progressively more negative as the initial subduction occurred earlier (Figure 7). This suggests that a longer subduction history, thus a greater length of the downgoing slab, exerts a stronger downward pull and exacerbate depressurization of the mantle above the slab. Consequently, this leads to a greater dynamic pressure-gradient across the slab, which, by preferentially affecting the upper-mantle portion of the slab, causes continuous reduction in the slab dip angle over time. A more quantitative analysis of this mechanical process is presented later in the discussion part. This reasoning is also consistent with the steady increase of pressure-gradient across the slab and temporal decrease of slab dip angle during the Cretaceous in the reference model (Figure 6). Mechanically, the scenarios in Figures 6a and 6b are similar to the proposed shallowing of the South American slab from the Cretaceous to the Cenozoic (Schellart, 2017). Furthermore, our study explains the recent finding that the subduction duration negatively correlates with the slab dip angle observed at the present day (Hu & Gurnis, 2020) and is consistent with a recent regional study (Schellart, 2020).

Regarding the formation of the Late-Cretaceous flat Izanagi slab, nearby subduction may also have played a role. Besides the western Pacific, another major subduction zone, the Tethyan trench along South Asia, has been active since the early Mesozoic (Müller et al., 2016). Although the Tethyan subducting slab was more segmented than
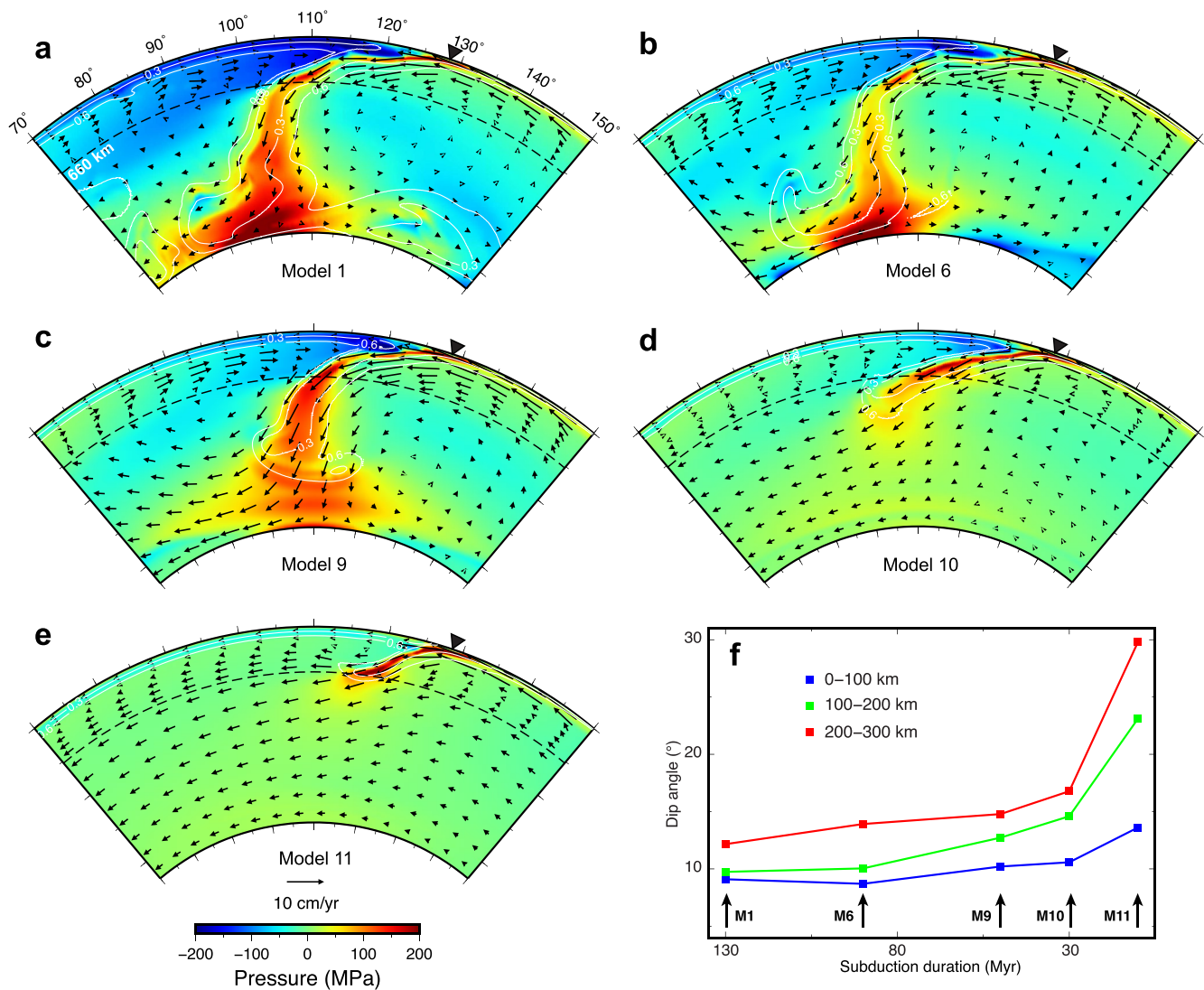
Figure 7. Variation of dynamic pressure and slab geometry with the starting age of subduction. (a–e) Distribution of dynamic pressure, mantle velocities and slabs along 32°N in Models 1, 6, and 9–11, respectively. The two levels of white contours within the slab mark non-dimensional temperature at 0.3 and 0.6, respectively. Black triangles show trench locations. (f) Horizontally averaged slab dip for each model (M1 for Model 1) at three different depth intervals. Color-coded squares show the mean dip angle at given depth ranges.

the Izanagi slab due to intervening terrane accretion, a broad low-pressure mantle region above the Tethyan slab formed prior to that above the Izanagi slab (Figure 6a), and the pressure also became progressively more negative over time (Figures 6b–6d). The Tethyan low-pressure zone expanded to merge with that along East Asia by ~140 Ma and excited notable westward flow beneath East Asia throughout the deep mantle since then (Figures 6 and S3). We suggest that this augmented hydrodynamic suction force across the East Asian subduction system further facilitated the ultimate flattening of the Izanagi slab during the Late Cretaceous (Figure 6).

An examination of global subduction suggests that most of the normal slab dip scenarios were associated with intermittent subduction or when the continuous slab length was small. For example, in South Asia and South America, the slabs were generally short with intermittent subduction periods, and the dip angles were large (Figures 1 and S3). For South America, the shallow slab dip angle decreased during the Cenozoic because of the continuous subduction (Figure S3). These are in contrast to the Izanagi slab (at 70 Ma) and the Farallon slab (at 40 Ma) that evolved into long, continental scale flat slabs, before which both regions had a continuous subduction duration of 130 Myr (Figures 1 and S3). Besides previous mechanisms for the flat Farallon slab such as oceanic plateau subduction (Liu et al., 2010) and fast overriding plate motion (Liu & Currie, 2016), this study suggests that the long

subduction duration may have also contributed to the flattening of the Farallon slab. These global slab behaviors further support our new mechanism that long prior subduction duration is important for flat subduction to occur, with a newly identified widespread flat slab below the Late Cretaceous East Asia (Figures 1 and 4).

3.5. Physical Mechanism for the Flat Izanagi Slab

To further understand the physical mechanism, we will take a closer look at the suction torque and gravity torque whose balance determines the slab dip angle. As shown above, the slab dip at shallow mantle depth strongly depends on subduction duration. This mechanism could be more quantitatively explained through the evolving force and torque balance between dynamic pressure and slab dip angle. For simplicity, we assume a stationary trench, where the slab subducts at velocity U, with a depth-invariant dip angle θ over a slab length L (Figure 8a). According to Stevenson and Turner (1977), the dynamic pressure at a given depth in the sub-slab region A is higher than that in the mantle wedge B, forming a pressure gradient across the slab, whose magnitude is positively correlated with U, negatively with θ, but independent of L. This pressure difference, when integrated along the slab length L, leads to a hydrodynamic suction torque (per unit trench length) defined around the trench:

$$T_H = 2\eta U L \left[\frac{\sin\theta}{(\pi - \theta) + \sin\theta} + \frac{\sin^2\theta}{\theta^2 - \sin^2\theta} \right]. \tag{6}$$

This torque tends to rotate the slab to reduce its dip θ. On the other hand, the gravity force due to negative buoyancy of the slab exerts an opposite-sensed torque

$$T_G = \frac{1}{2} b L^2 \cos\theta, \tag{7}$$

where b is the average negative buoyancy per unit slab area. The balance between T_H and T_G determine the slab dip θ, as shown in Figure 8b.

To understand the effect of slab length L on slab dip θ, we first define a reference scenario of torque balance: for a given value of L, there exists a value of b that satisfies $T_H = T_G$; this corresponds to a critical slab buoyancy $b_c \approx 20\eta U/L$ and to a critical dip angle $\theta_c \approx 63°$ (Stevenson & Turner, 1977). While the suction term ($T_H/2\eta U L$) in Figure 8 only depends on θ, the gravitational term is affected by more factors, including mantle viscosity (η), subduction rate (U), slab length (L), slab thickness and density. For convenience, we use the ratio $r_b = b/b_c$ to evaluate the torque balance. Assuming that mantle viscosity, subduction rate, slab thickness and density are constants during subduction, the ratio r_b will depend only on slab length L. As L increases, b becomes larger than b_c, which will result in two balancing points, one with a smaller dip angle and the other with a larger dip angle. These two balancing points will move progressively away from θ_c as L keeps increasing, with the slab eventually becoming flat ($\theta = 0°$) or vertical ($\theta = 90°$).

We suggest that the latter case (θ evolves toward 90° as L increases) is unlikely for East Asian subduction. For this scenario to occur, the initial slab dip needs to reach the critical value of 63°. Here this initial condition should be a scenario when L is significantly larger than the slab thickness, in order to satisfy the thin-slab assumption (Stevenson & Turner, 1977). As recent studies demonstrate, the slab is relatively steep before its downdip end gets anchored in the high-viscosity lower mantle (e.g., Schellart, 2017), and the depth-averaged slab dip in this case usually stays significantly lower than 60° (Hu & Gurnis, 2020). For East Asia, the dip angle was large prior to 160 Ma due to the fast trench advance (Figure S1). However, after that the slab dip angle slowly decreased. From 140 to 120 Ma, the average upper-mantle slab dip kept less than 45° (e.g., Figure S3). Consequently, the subsequent torque balance as subduction continues will evolve toward lowering instead of increasing the slab dip (Figure 8b). It is notable that this torque balance promotes positive feedback between the reducing slab dip and dynamic suction (Figure 8b), which facilitates the eventual formation of a flat slab (Figures 6 and S3). In reality, slabs are not infinitely rigid as assumed here. Therefore, the increasing suction torque with growing L will cause the slab to internally bend, a process that should follow the local dynamic pressure gradient. The observed increasing pressure gradient with decreasing depth (Figures 6 and 7) means that the shallowest slab is most susceptible to flattening (Figure S3). This is also consistent with the finding that the slab above 300 km depth demonstrates the strongest dependence on the accumulating dynamic pressure over time (Figure 7).
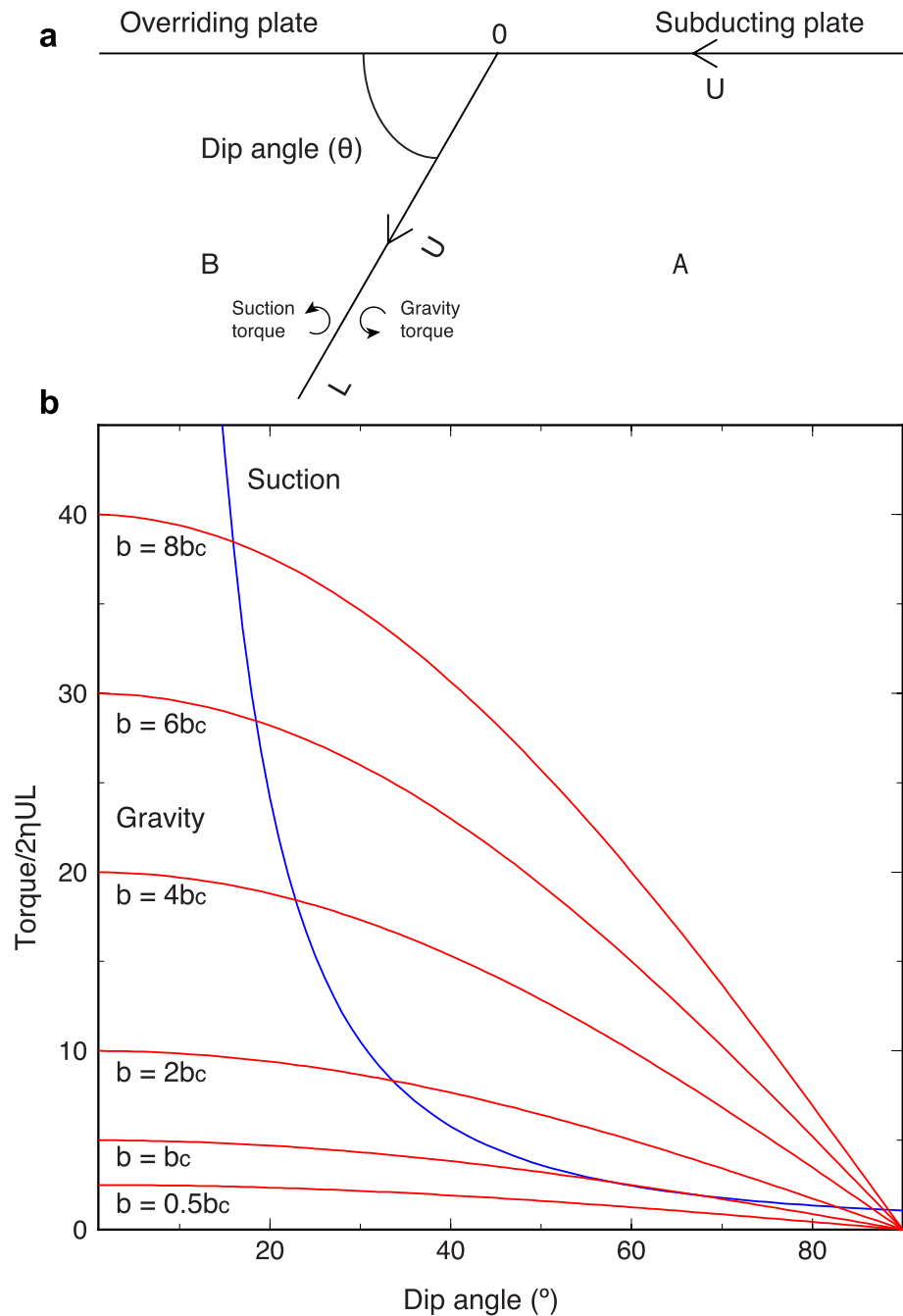
Figure 8. Slab torque balance and its effect on slab dip angle. (a) A simplified subduction system with a fixed trench, a subduction rate of U and a slab length of L. Zone A and zone B experience positive and negative dynamic pressure, forming a pressure-gradient across the slab. (b) The balance between the suction torque (blue) and the gravity torque (red) as slab buoyancy (via L) changes determines the slab dip angle. The critical slab dip and buoyancy are defined as when there is only one solution in slab dip for the torque balance.

Besides the balance of gravity torque and suction torque as discussed before, there are other factors that may effect the slab dip angle as well, including a global scale eastward upper-mantle flow (Doglioni, 1990) and toroidal flow around slab edges (Liu & Stegman, 2011; Schellart et al., 2007). However, a global scale west to east mantle flow tends to increase the dip angle of the Izanagi slab, opposite to the westward flattening of the slab that represents a robust result in this study. Thus, we suggest such an eastward global upper-mantle flow should not exist. The toroidal flow, on the other hand, mainly affects the dip angel near the edges of the slab. For a wide subduction

zone like in this study, the width of the trench is enormous and the region we focused on is far away from all the edges (Figure 1). So, the toroidal flow should not play an important role in the flat Izanagi subduction as well.

Consequently, the mechanism for this newly discovered Late-Cretaceous Izanagi flat slab represents a combination of two existing hypotheses: the long-existing prior subduction gradually builds up the hydrodynamic suction force within the mantle wedge that eventually leads to the continental-scale flat slab beneath East Asia. Therefore, both our discovery of the flat East Asian slab and its physical mechanism present new knowledge to the field of geodynamics and tectonics.

4. Discussion

4.1. Advantages and Limitations of the Models

In this study, all the models are thermal-chemical global models which are more realistic than previous models. In addition to the resulting asymmetric subduction, our models are also capable to capture the variations of slab dip angles in response to changes of the dynamic pressure gradient across the slab (Figures 6 and 7). Previous global models either have subvertical slabs due to the pure-thermal nature (e.g., Mao & Zhong, 2018) or have predefined shallow slab dip angle (e.g., Ma et al., 2019). These limitations make it impossible to simulate the temporal evolution of flat slabs. Some earlier 2D models have freely evolving slab dip angles (e.g., Liu & Currie, 2016). These models can represent the general behavior of flat subduction, but the 2D nature makes it difficult for the model to be directly compared to observations. For example, our model predicted slab flattening and lithospheric thinning east of the NSGL from Northeast China to South China but with clear spatial variations, closely following the observation. This geographically oriented model predictions cannot be produced within 2D models.

On the other hand, there are some potential limitations in our models. First, we assume an incompressible mantle using Boussinesq approximation. Recent studies showed that models with a compressible mantle generally have thinner lower-mantle slabs than incompressible models (Flament, 2019). In this study, we focus on the behavior of upper-mantle slabs, and we suspect mantle compressibility may have a small effect on flat slab formation. Although in reality the lower-mantle slabs may be thinner than modeled here, the net effect on slab dip angle at shallow depth may be small, because when the gravity torque of the sinking slab is smaller due to reduced slab buoyancy, the pressure difference across the slab (the suction torque) is also reduced due to the reduced slab sinking rate, maintaining a similar torque balance (Figure 8). This can be partially shown by the test that different slab ages (thus difference slab thicknesses and gravity torque) result in similar geometry of the flat slab (Figures 5a and 5f).

Second, we assume the CMB temperature to be 500°C higher than ambient in most of the models, lower than that used in some previous studies (Flament, 2019; Hassan et al., 2016; Zhang & Li, 2018). This temperature setting, combined with the chemically dense compositional layer above the CMB, leads to a net positive density of the hot CMB composition pile, which is consistent with previous studies (Lau et al., 2017). Overall, the uncertain chemical density of this basal composition layer renders its true temperature anomaly poorly constrained. On the other hand, given the great distance of the CMB from the surface, we suggest its temperature should have little effect on upper-mantle slab dynamics. Indeed, Model 12, with a higher CMB temperature, produced a similar flat Izanagi slab as that in Model 1 (Figure S10), confirming that the CMB temperature does not affect the overall geometry of the flat Izanagi slab.

4.2. Lithospheric and Surface Responses of the Flat Izanagi Subduction

We propose that the observed lithospheric thinning east of the NSGL, the Late-Cretaceous termination of sedimentation within eastern China basins but rapid subsidence within Sichuan Basin further west, and the contemporaneous uplift of Greater Xing'an-Taihang-Xuefeng mountains all reflect different aspects of the lithospheric and surface responses during the flat Izanagi subduction. These geological implications are consistent with previous studies which suggest that flat subduction could cause orogenic uplift (Espurt et al., 2008; Liu et al., 2010) and lithospheric thinning (Axen et al., 2018; Bird, 1988). There are other proposed mechanisms for the formation of the NSGL, among which is the stagnant slab induced lithospheric thinning and craton destruction (e.g., Liu et al., 2019; Xu, 2007). Recent modeling studies show that the presently observed stagnant slab did not form until the Miocene (Ma et al., 2019; Mao & Zhong, 2018), too late compared to these Mesozoic tectonic events. The
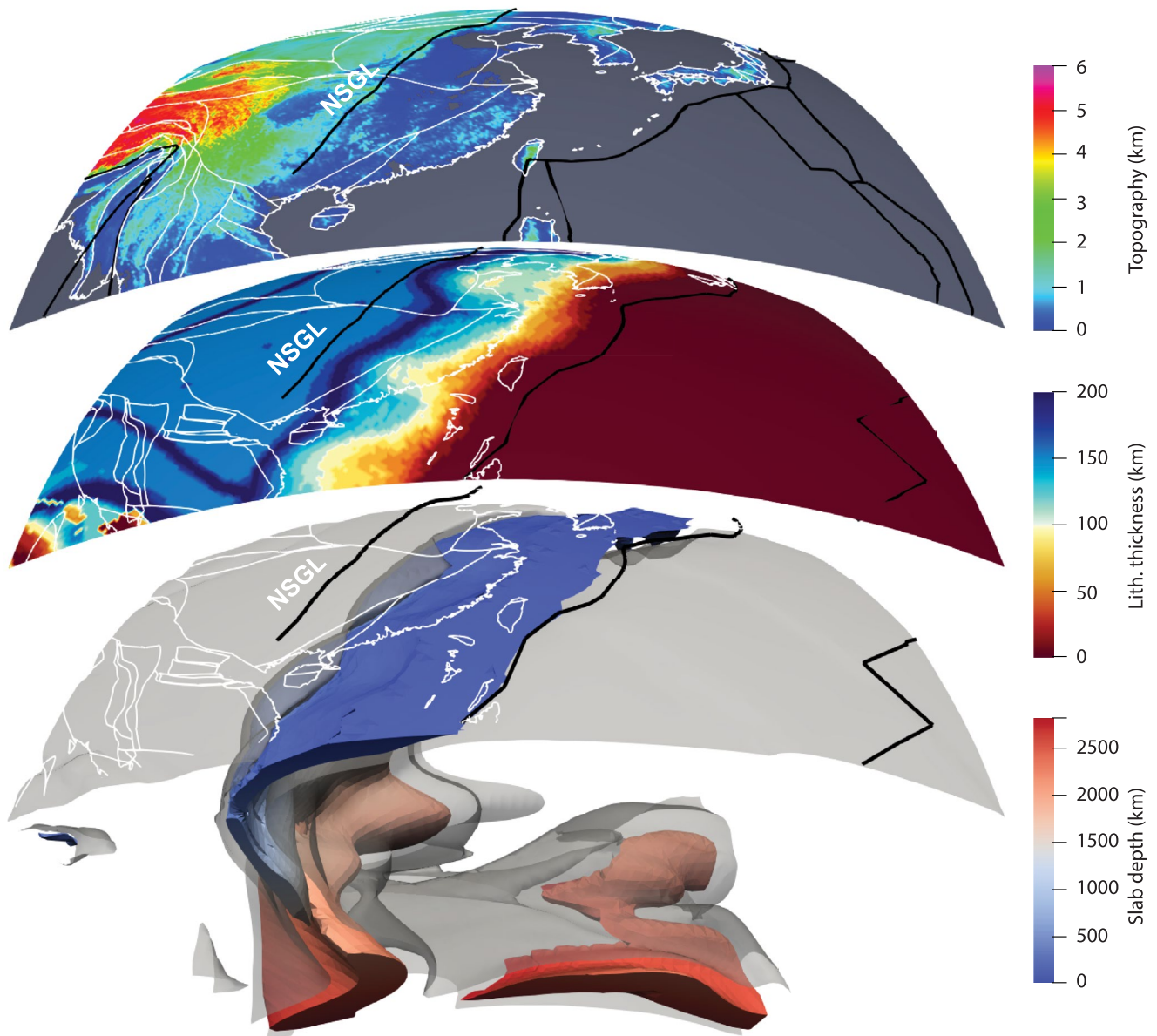
Figure 9. Flat slab, continental lithosphere thickness and topography. The slab geometry (bottom) and continental lithosphere thickness (middle) at 70 Ma are plotted against the present-day topography (top). The slab is shown as a volume at the inner part with the nondimensional temperature lower than 0.2 (color denoting slab depth) and an isosurface of temperature at 0.45 at the outer part. Continental lithospheric thickness is calculated by tracing the composition of the lower lithosphere. The NSGL is shown as the thick black line. Plate boundaries (thick black lines), coastlines and tectonic outlines (thin white lines) were rotated following the continent based on plate kinematics (Müller et al., 2016) for comparison between 70 Ma and the present day.

Late-Cretaceous flat Izanagi slab provides an alternative mechanism, as summarized in Figure 9, where the spatial extents of the flat slab, the thinned lithosphere and the low present-day elevation east of the NSGL strongly correlate with each other.

A common surface response during flat slab subduction is abnormal arc magmatism (Gutscher et al., 2000; Henderson et al., 1984; L. Liu et al., 2021). Within East Asia, widespread intraplate volcanisms, much of which had an arc affinity, sustained since the middle Mesozoic. These volcanisms rapidly waned during the Late Cretaceous and disappeared throughout most of East Asia by 80 Ma (Li, 2000; L. Liu et al., 2021; Liu et al., 2020; Tang et al., 2018; Zhou & Li, 2000). A definitive mechanism for this continental-scale magmatic shutdown is still lacking. Based on the match with many other independent Late-Cretaceous tectonic events, we suggest that our

flat slab model provides an intuitive solution: During the period of flat subduction, the replacement of the former hot mantle wedge by the cold flat oceanic slab shut down preexisting volcanisms, forming a widespread and long-lasting magmatic lull.

The topographic evolution during flat slab subduction is another topic of research. We propose that the observed Late-Cretaceous uplift and basin inversion within East Asia was caused by the flat Izanagi slab right below and that the contemporarily enhanced subsidence in the Sichuan Basin further west reflects dynamic topography above the leading edge of the slab. We note that this topographic expression of the flat slab is not universally true. For example, the flat Farallon slab resulted in widespread subsidence both above and beyond the flat portion, with uplift commencing after the passage of the slab (Chang & Liu, 2021; Heller & Liu, 2016; Liu et al., 2011). In this case, surface topography mostly represented dynamic topography due to sub-lithospheric convection, while the cratonic upper plate that experienced little crustal thickening contributed little to surface topography. We suggest that the different topographic response of East Asia right above the flat slab reflects its weaker lithosphere that is easier to shorten and deform (Figures 4 and 9) than cratons, with the resulting isostatic uplift dominating the slab-induced dynamic subsidence.

However, we realize that there is still little consensus on the mechanisms of topography variation during flat subduction, due to the debated topographic contributions of the flat slab itself and of upper-plate deformation. Some researchers assumed the flat slab to be neutrally buoyant whose landward migration causes dynamic uplift instead of subsidence (Dávila & Lithgow-Bertelloni, 2015). It is worth noting that flat subduction does not require a neutrally buoyant slab (this study). Alternatively, reduced subsidence due to slab tearing or breakoff during shallow to flat subduction could also result in surface uplift (Flament et al., 2015; Liu & Stegman, 2012; Zhou & Liu, 2019). Another apparent complication is the contribution from isostatic topography due to upper-plate deformation (e.g., Bird, 1988), an important aspect that many recent flat-slab models failed to consider. This missing component could be very important for non-cratonic upper plate such as East Asia, where both the removal of the lower lithosphere (Figure 4) and crustal shortening (Bird, 1988) may significantly affect surface topography. In addition, one common practice for estimating dynamic topography usually removes all shallow (e.g., <300 km depth) mantle density anomalies (Flament et al., 2015; Yang & Gurnis, 2016; Zhou & Liu, 2019), which in the case of flat subduction may omit the topographic effect of the entire flat slab segment that is usually within this depth range. Considering these existing discrepancies, we suggest more research is needed to better address this problem.

4.3. Comparison With Other Flat Slabs

In this study, our models predicted the present-day flat Nazca slab and Late-Cretaceous Izanagi slab and Farallon slab (Figures 1 and S3). The most prominent ones are Izanagi and Farallon slabs with the flat part of the former being the longest in the trench-normal direction (Figure 1). Besides the mechanisms of flat slab formation discussed above, there are other potential factors affecting the dip angle of the Izanagi slab. First, the subduction speed of the Izanagi Plate had been large during the Late Mesozoic (Figure S7). This could help maintain a strong suction torque across the slab (Equation 6), facilitating slab flattening. Second, the adjacent Tethyan subduction could enhance depressurization within the mantle below East Asia. This became especially relevant as both the Izanagi and Tethyan slabs reach the deep mantle, when the mechanically strong slabs finally enclosed the East Asian mantle to build up the low-pressure region landward of the downgoing slabs (Figure 6). In our model, the Tethyan and Izanagi slabs touched each other to form a continuous mantle wall from South Asia to East Asia at about 100 Ma. This time is also when the Izanagi slab started to flatten. A recent study implied that the Tethyan slab had a temporary shallow slab dip during 85–65 Ma (X. Zhang et al., 2019), a process also reproduced in our model (Figure 1). This time also closely correlates with the peak stage of the flat Izanagi slab during 80–60 Ma (Figure 4), consistent with the enhanced suction across these two giant slabs due to their mutual interaction at depth (Figure 6).

The Mesozoic subduction history below the eastern Pacific is similar to that below the western Pacific in that subduction is continuous since the Late Mesozoic, with a decreasing seafloor age over time and relatively large subduction rate (Müller et al., 2016). There are also some differences between them. First, North America migrated westward for a long distance (>2,000 km) during this period, while there was not much trench-ward migration of Eurasia (e.g., Müller et al., 2016). Second, the N-S oriented Farallon slab represents a dominant subduction system in the region without adjacent slabs. While the first difference may facilitate flat subduction through

enhancing the suction torque (Figure 8; van Hunen et al., 2000), the second difference favors a steeper Farallon slab than the Izanagi slab (Figure 6). Consequently, the relatively shorter flat Farallon slab than the Izanagi slab both in the numerical model (Figure 1) and implied by tectonic responses (Figure 3) suggests that the effect of overriding plate motion plays a relatively minor role in slab flattening.

The lateral dimensions of flat slabs also differ. The Late-Cretaceous Izanagi flat slab covered a very wide range (>2,000 km) along the trench (Figure 4). The Farallon flat slab was also very wide as required by the continental scale Cretaceous Seaway (Liu et al., 2008), but its flattest portion was restricted to within the western United States (Saleeby, 2003), likely representing a subducting oceanic plateau (Liu et al., 2010). In contrast, the present Nazca slab below South America is flattened mostly near the subducting aseismic ridges (Hu et al., 2016) and/or nearby cratonic roots (Manea et al., 2012; Taramón et al., 2015). Better quantification of the effects of different mechanisms in controlling the 3-D geometry of flat slabs represents another topic of future work.

5. Conclusion

1. In this study, we investigated the Mesozoic subduction of the western Pacific with global data-assimilation models. A robust model result is the flattening of the Izanagi slab during the Late Cretaceous as long as western Pacific subduction started prior to the Cretaceous. This represents a previously unrecognized subduction scenario.
2. The flat Izanagi subduction is largely independent of the chosen plate reconstruction, continental lithospheric thickness, convergence rate and seafloor age variation. The key mechanism for this flat slab is the former slabs generated along the same and nearby subduction zones.
3. The flat Izanagi slab provides a new mechanism for the formation of the NSGL. During the flat subduction, the lower lithosphere of East Asia was removed by the slab. This resulted in a thinned lithosphere to the east of the NSGL, consistent with seismic studies.
4. The flat Izanagi slab could also explain the widespread Late-Cretaceous tectonic inversion of major sedimentary basins east of the NSGL and the synchronously enhanced subsidence of the Sichuan Basin to the west.
5. The Greater Xing'an-Taihang-Xuefeng mountains along the NSGL experienced simultaneous Late-Cretaceous uplift and exhumation, likely reflecting severe crustal shortening along the front of the flat Izanagi slab.

Data Availability Statement

Most figures are prepared with GMT (https://www.generic-mapping-tools.org/) and Paraview (https://www.paraview.org/). Surface velocity and plate boundary files are exported using Gplates (https://www.gplates.org/). The original version of CitcomS is available at www.geodynamics.org/cig/software/citcoms/. The P wave tomography model UU-P07 is available at https://www.atlas-of-the-underworld.org/uu-p07-model/. MIT-P08 is within the study (Li et al., 2008) and its Supporting Information S1. GAP-P4 is available at http://d-earth.jamstec.go.jp/GAP_P4/. The S wave tomography model SEMUCB-WM1 is available is at http://seismo.berkeley.edu/wiki_br/. S40RTS is available at https://jritsema.earth.lsa.umich.edu/Research.html.

References

Amaru, M. L. (2007). Global travel time tomography with 3-D reference models. In *Geologica Ultraiectina* (pp. 1–174). Utrecht University.

Axen, G. J., van Wijk, J. W., & Currie, C. A. (2018). Basal continental mantle lithosphere displaced by flat-slab subduction. *Nature Geoscience*, *11*(12), 961–964. https://doi.org/10.1038/s41561-018-0263-9

Becker, T. W., & Boschi, L. (2002). A comparison of tomographic and geodynamic mantle models. *Geochemistry, Geophysics, Geosystems*, *3*(1), 1. https://doi.org/10.1029/2001GC000168

Bird, P. (1988). Formation of the Rocky Mountains, Western United States: A continuum computer model. *Science*, *239*(4847), 1501–1507. https://doi.org/10.1126/science.239.4847.1501

Bond, G. (1976). Evidence for continental subsidence in North America during the Late Cretaceous global submergence. *Geology*, *4*(9), 557. https://doi.org/10.1130/0091-7613(1976)4<557:EFCSIN>2.0.CO;2

Bunge, H., & Grand, S. P. (2000). Mesozoic plate-motion history below the northeast Pacific Ocean from seismic images of the subducted Farallon slab. *Nature*, *405*(6784), 337–340. https://doi.org/10.1038/35012586

Chang, C., & Liu, L. (2021). Investigating the formation of the Cretaceous Western Interior Seaway using landscape evolution simulations. *GSA Bulletin*, *133*(1–2), 347–361. https://doi.org/10.1130/B35653.1

Chen, L., Jiang, M., Yang, J., Wei, Z., Liu, C., & Ling, Y. (2014). Presence of an intralithospheric discontinuity in the central and western North China Craton: Implications for destruction of the craton. *Geology*, *42*(3), 223–226. https://doi.org/10.1130/G35010.1

Clinkscales, C., Kapp, P., & Wang, H. (2020). Exhumation history of the north-central Shanxi Rift, North China, revealed by low-temperature thermochronology. *Earth and Planetary Science Letters*, *536*, 116146. https://doi.org/10.1016/j.epsl.2020.116146

Coltice, N., Husson, L., Faccenna, C., & Arnould, M. (2019). What drives tectonic plates? *Science Advances*, *5*(10), eaax4295. https://doi.org/10.1126/sciadv.aax4295

Coney, P. J., & Reynolds, S. J. (1977). Cordilleran Benioff zones. *Nature*, *270*(5636), 403–406. https://doi.org/10.1038/270403a0

Dávila, F. M., & Lithgow-Bertelloni, C. (2015). Dynamic uplift during slab flattening. *Earth and Planetary Science Letters*, *425*, 34–43. https://doi.org/10.1016/j.epsl.2015.05.026

DeCelles, P. G. (2004). Late Jurassic to Eocene evolution of the Cordilleran thrust belt and foreland basin system, western USA. *American Journal of Science*, *304*(2), 105–168. https://doi.org/10.2475/ajs.304.2.105

Doglioni, C. (1990). The global tectonic pattern. *Journal of Geodynamics*, *12*(1), 21–38. https://doi.org/10.1016/0264-3707(90)90022-M

English, J. M., Johnston, S. T., & Wang, K. (2003). Thermal modelling of the Laramide orogeny: Testing the flat-slab subduction hypothesis. *Earth and Planetary Science Letters*, *214*(3–4), 619–632. https://doi.org/10.1016/S0012-821X(03)00399-6

Espurt, N., Funiciello, F., Martinod, J., Guillaume, B., Regard, V., Faccenna, C., & Brusset, S. (2008). Flat subduction dynamics and deformation of the South American plate: Insights from analog modeling. *Tectonics*, *27*(3), 1. https://doi.org/10.1029/2007TC002175

Fan, M., & Carrapa, B. (2014). Late Cretaceous-early Eocene Laramide uplift, exhumation, and basin subsidence in Wyoming: Crustal responses to flat slab subduction. *Tectonics*, *33*(4), 509–529. https://doi.org/10.1002/2012TC003221

Flament, N. (2019). Present-day dynamic topography and lower-mantle structure from palaeogeographically constrained mantle flow models. *Geophysical Journal International*, *216*(3), 2158–2182. https://doi.org/10.1093/gji/ggy526

Flament, N., Gurnis, M., Müller, R. D., Bower, D. J., & Husson, L. (2015). Influence of subduction history on South American topography. *Earth and Planetary Science Letters*, *430*, 9–18. https://doi.org/10.1016/j.epsl.2015.08.006

French, S. W., & Romanowicz, B. A. (2014). Whole-mantle radially anisotropic shear velocity structure from spectral-element waveform tomography. *Geophysical Journal International*, *199*(3), 1303–1327. https://doi.org/10.1093/gji/ggu334

Ge, X., Shen, C., Selby, D., Deng, D., & Mei, L. (2016). Apatite fission-track and Re-Os geochronology of the Xuefeng uplift, China: Temporal implications for dry gas associated hydrocarbon systems. *Geology*, *44*(6), 491–494. https://doi.org/10.1130/G37666.1

Gutscher, M.-A., Spakman, W., Bijwaard, H., & Engdahl, E. R. (2000). Geodynamics of flat subduction: Seismicity and tomographic constraints from the Andean margin. *Tectonics*, *19*(5), 814–833. https://doi.org/10.1029/1999TC001152

Hassan, R., Müller, R. D., Gurnis, M., Williams, S. E., & Flament, N. (2016). A rapid burst in hotspot motion through the interaction of tectonics and deep mantle flow. *Nature*, *533*(7602), 239–242. https://doi.org/10.1038/nature17422

Hayes, G. P., Wald, D. J., & Johnson, R. L. (2012). Slab1.0: A three-dimensional model of global subduction zone geometries. *Journal of Geophysical Research*, *117*(1), 1. https://doi.org/10.1029/2011JB008524

Heller, P. L., & Liu, L. (2016). Dynamic topography and vertical motion of the U.S. Rocky Mountain region prior to and during the Laramide orogeny. *The Geological Society of America Bulletin*, *128*(5–6), 973–988. https://doi.org/10.1130/B31431.1

Henderson, L. J., Gordon, R. G., & Engebretson, D. C. (1984). Mesozoic aseismic ridges on the Farallon Plate and southward migration of shallow subduction during the Laramide Orogeny. *Tectonics*, *3*(2), 121–132. https://doi.org/10.1029/TC003i002p00121

Hu, J., & Gurnis, M. (2020). Subduction duration and slab dip. *Geochemistry, Geophysics, Geosystems*, *21*(4), 1–24. https://doi.org/10.1029/2019GC008862

Hu, J., & Liu, L. (2016). Abnormal seismological and magmatic processes controlled by the tearing South American flat slabs. *Earth and Planetary Science Letters*, *450*, 40–51. https://doi.org/10.1016/j.epsl.2016.06.019

Hu, J., Liu, L., Faccenda, M., Zhou, Q., Fischer, K. M., Marshak, S., & Lundstrom, C. (2018). Modification of the Western Gondwana craton by plume-lithosphere interaction. *Nature Geoscience*, *11*(3), 203–210. https://doi.org/10.1038/s41561-018-0064-1

Hu, J., Liu, L., Hermosillo, A., & Zhou, Q. (2016). Simulation of late Cenozoic South American flat-slab subduction using geodynamic models with data assimilation. *Earth and Planetary Science Letters*, *438*, 1–13. https://doi.org/10.1016/j.epsl.2016.01.011

Hu, J., Liu, L., & Zhou, Q. (2018). Reproducing past subduction and mantle flow using high-resolution global convection models. *Earth and Planetary Physics*, *2*(3), 189–207. https://doi.org/10.26464/epp2018019

Huangfu, P., Wang, Y., Cawood, P. A., Li, Z. H., Fan, W., & Gerya, T. V. (2016). Thermo-mechanical controls of flat subduction: Insights from numerical modeling. *Gondwana Research*, *40*, 170–183. https://doi.org/10.1016/j.gr.2016.08.012

Jones, C. (2012). Hydrodynamic mechanism for the Laramide orogeny. *Geosphere*, *7*(1), 183. https://doi.org/10.1130/GES00575.1

Kapp, P., & Decelles, P. G. (2019). Mesozoic-Cenozoic geological evolution of the Himalayan-Tibetan orogen and working tectonic hypotheses. *American Journal of Science*, *319*(3), 159–254. https://doi.org/10.2475/03.2019.01

Lau, H. C. P., Mitrovica, J. X., Davis, J. L., Tromp, J., Yang, H.-Y., & Al-Attar, D. (2017). Tidal tomography constrains Earth's deep-mantle buoyancy. *Nature*, *551*(7680), 321–326. https://doi.org/10.1038/nature24452

Li, C., van der Hilst, R. D., Meltzer, A. S., & Engdahl, E. R. (2008). Subduction of the Indian lithosphere beneath the Tibetan Plateau and Burma. *Earth and Planetary Science Letters*, *274*(1–2), 157–168. https://doi.org/10.1016/j.epsl.2008.07.016

Li, X. H. (2000). Cretaceous magmatism and lithospheric extension in Southeast China. *Journal of Asian Earth Sciences*, *18*(3), 293–305. https://doi.org/10.1016/S1367-9120(99)00060-7

Li, Y., Gao, M., & Wu, Q. (2014). Crustal thickness map of the Chinese mainland from teleseismic receiver functions. *Tectonophysics*, *611*, 51–60. https://doi.org/10.1016/j.tecto.2013.11.019

Li, Y., He, D., Chen, L., Mei, Q., Li, C., & Zhang, L. (2016). Cretaceous sedimentary basins in Sichuan, SW China: Restoration of tectonic and depositional environments. *Cretaceous Research*, *57*, 50–65. https://doi.org/10.1016/j.cretres.2015.07.013

Li, Z. X., & Li, X. H. (2007). Formation of the 1300-km-wide intracontinental orogen and postorogenic magmatic province in Mesozoic South China: A flat-slab subduction model. *Geology*, *35*(2), 179–182. https://doi.org/10.1130/G23193A.1

Liu, J., Cai, R., Pearson, D. G., & Scott, J. M. (2019). Thinning and destruction of the lithospheric mantle root beneath the North China Craton: A review. *Earth-Science Reviews*, *196*, 102873. https://doi.org/10.1016/j.earscirev.2019.05.017

Liu, L. (2015). The ups and downs of North America: Evaluating the role of mantle dynamic topography since the Mesozoic. *Reviews of Geophysics*, *53*(3), 1022–1049. https://doi.org/10.1002/2015RG000489

Liu, L., Gurnis, M., Seton, M., Saleeby, J., Müller, R. D., & Jackson, J. M. (2010). The role of ,oceanic plateau subduction in the Laramide orogeny. *Nature Geoscience*, *3*(5), 353–357. https://doi.org/10.1038/ngeo829

Liu, L., Liu, L., & Xu, Y. G. (2021). Mesozoic intraplate tectonism of East Asia due to flat subduction of a composite terrane slab. *Earth-Science Reviews*, *214*, 103505. https://doi.org/10.1016/j.earscirev.2021.103505

Liu, L., Spasojević, S., & Gurnis, M. (2008). Reconstructing Farallon plate subduction beneath North America back to the Late Cretaceous. *Science*, *322*(5903), 934–938. https://doi.org/10.1126/science.1162921

Liu, L., & Stegman, D. R. (2011). Segmentation of the Farallon slab. *Earth and Planetary Science Letters*, *311*(1–2), 1–10. https://doi.org/10.1016/j.epsl.2011.09.027

Liu, L., & Stegman, D. R. (2012). Origin of Columbia River flood basalt controlled by propagating rupture of the Farallon slab. *Nature*, *482*(7385), 386–389. https://doi.org/10.1038/nature10749

Liu, L. J., Peng, D., Liu, L., Chen, L., Li, S., Wang, Y., et al. (2021). East Asian lithospheric evolution dictated by multistage Mesozoic flat-slab subduction. *Earth-Science Reviews*, *217*, 103621. https://doi.org/10.1016/j.earscirev.2021.103621

Liu, M., Cui, X., & Liu, F. (2004). Cenozoic rifting and volcanism in eastern China: A mantle dynamic link to the Indo-Asian collision? *Tectonophysics*, *393*, 29–42. https://doi.org/10.1016/j.tecto.2004.07.029

Liu, S., & Currie, C. A. (2016). Farallon plate dynamics prior to the Laramide orogeny: Numerical models of flat subduction. *Tectonophysics*, *666*, 33–47. https://doi.org/10.1016/j.tecto.2015.10.010

Liu, S., Gurnis, M., Ma, P., & Zhang, B. (2017). Reconstruction of northeast Asian deformation integrated with western Pacific plate subduction since 200 Ma. *Earth-Science Reviews*, *175*, 114–142. https://doi.org/10.1016/j.earscirev.2017.10.012

Liu, S., Nummedal, D., & Liu, L. (2011). Migration of dynamic subsidence across the Late Cretaceous United States Western Interior Basin in response to Farallon plate subduction. *Geology*, *39*(6), 555–558. https://doi.org/10.1130/G31692.1

Liu, Y., Liu, L., Wu, Z., Li, W., & Hao, X. (2020). New insight into East Asian tectonism since the late Mesozoic inferred from erratic inversions of NW-trending faulting within the Bohai Bay Basin. *Gondwana Research*. https://doi.org/10.1016/j.gr.2020.01.022

Ma, P., Liu, S., Gurnis, M., & Zhang, B. (2019). Slab horizontal subduction and slab tearing beneath East Asia. *Geophysical Research Letters*, *46*(10), 5161–5169. https://doi.org/10.1029/2018GL081703

Manea, V. C., Pérez-Gussinyé, M., & Manea, M. (2012). Chilean flat slab subduction controlled by overriding plate thickness and trench rollback. *Geology*, *40*(1), 35–38. https://doi.org/10.1130/G32543.1

Mao, W., & Zhong, S. (2018). Slab stagnation due to a reduced viscosity layer beneath the mantle transition zone. *Nature Geoscience*, *11*(11), 876–881. https://doi.org/10.1038/s41561-018-0225-2

Mao, W., & Zhong, S. (2019). Controls on global mantle convective structures and their comparison with seismic models. *Journal of Geophysical Research: Solid Earth*, *124*(8), 9345–9372. https://doi.org/10.1029/2019JB017918

Marquardt, H., & Miyagi, L. (2015). Slab stagnation in the shallow lower mantle linked to an increase in mantle viscosity. *Nature Geoscience*, *8*(4), 311–314. https://doi.org/10.1038/ngeo2393

McNamara, A. K., & Zhong, S. (2004). Thermochemical structures within a spherical mantle: Superplumes or piles? *Journal of Geophysical Research*, *109*(B7), 1–14. https://doi.org/10.1029/2003JB002847

Müller, R. D., Seton, M., Zahirovic, S., Williams, S. E., Matthews, K. J., Wright, N. M., et al. (2016). Ocean basin evolution and global-scale plate reorganization events since pangea breakup. *Annual Review of Earth and Planetary Sciences*, *44*(1), 107–138. https://doi.org/10.1146/annurev-earth-060115-012211

Müller, R. D., Zahirovic, S., Williams, S. E., Cannon, J., Seton, M., Bower, D. J., et al. (2019). A global plate model including lithospheric deformation along major rifts and orogens since the Triassic. *Tectonics*, *38*(6), 1884–1907. https://doi.org/10.1029/2018TC005462

Obayashi, M., Yoshimitsu, J., Nolet, G., Fukao, Y., Shiobara, H., Sugioka, H., et al. (2013). Finite frequency whole mantle P wave tomography: Improvement of subducted slab images. *Geophysical Research Letters*, *40*(21), 5652–5657. https://doi.org/10.1002/2013GL057401

Pang, Y., Guo, X., Zhang, X., Zhu, X., Hou, F., Wen, Z., & Han, Z. (2020). Late Mesozoic and Cenozoic tectono-thermal history and geodynamic implications of the Great Xing'an Range, NE China. *Journal of Asian Earth Sciences*, *189*, 104155. https://doi.org/10.1016/j.jseaes.2019.104155

Qing, J. C., Ji, J. Q., Wang, J. D., Peng, Q. L., Niu, X. L., & Ge, Z. H. (2008). Apatite fission track study of Cenozoic uplifting and exhumation of Wutai Mountain, China. *Acta Geophysica Sinica*, *51*(2), 384–392. https://doi.org/10.1002/cjg2.1217

Ritsema, J., Deuss, A., Van Heijst, H. J., & Woodhouse, J. H. (2011). S40RTS: A degree-40 shear-velocity model for the mantle from new Rayleigh wave dispersion, teleseismic traveltime and normal-mode splitting function measurements. *Geophysical Journal International*, *184*(3), 1223–1236. https://doi.org/10.1111/j.1365-246X.2010.04884.x

Rudolph, M. L., Leki, V., & Lithgow-Bertelloni, C. (2015). Viscosity jump in Earths mid-mantle. *Science*, *350*(6266), 1349–1352. https://doi.org/10.1126/science.aad1929

Saleeby, J. (2003). Segmentation of the Laramide Slab—Evidence from the southern Sierra Nevada region. *Bulletin of the Geological Society of America*, *115*(6), 655–668. https://doi.org/10.1130/0016-7606(2003)115<0655:SOTLSF>2.0.CO;2

Schellart, W. P. (2017). Andean mountain building and magmatic arc migration driven by subduction-induced whole mantle flow. *Nature Communications*, *8*(1), 1–13. https://doi.org/10.1038/s41467-017-01847-z

Schellart, W. P. (2020). Control of subduction zone age and size on flat slab subduction. *Frontiers of Earth Science*, *8*, 1–18. https://doi.org/10.3389/feart.2020.00026

Schellart, W. P., Freeman, J., Stegman, D. R., Moresi, L., & May, D. (2007). Evolution and diversity of subduction zones controlled by slab width. *Nature*, *446*(7133), 308–311. https://doi.org/10.1038/nature05615

Seton, M., Müller, R. D., Zahirovic, S., Gaina, C., Torsvik, T., Shephard, G., et al. (2012). Global continental and ocean basin reconstructions since 200 Ma. *Earth-Science Reviews*, *113*(3–4), 212–270. https://doi.org/10.1016/j.earscirev.2012.03.002

Song, Y., Ren, J., Stepashko, A. A., & Li, J. (2014). Post-rift geodynamics of the Songliao Basin, NE China: Origin and significance of T11 (Coniacian) unconformity. *Tectonophysics*, *634*, 1–18. https://doi.org/10.1016/j.tecto.2014.07.023

Stevenson, D. J., & Turner, J. S. (1977). Angle of subduction. *Nature*, *270*(5635), 334–336. https://doi.org/10.1038/270334a0

Sun, W., & Kennett, B. L. N. (2017). Mid-lithosphere discontinuities beneath the western and central North China Craton. *Geophysical Research Letters*, *44*(3), 1302–1310. https://doi.org/10.1002/2016GL071840

Tan, E., Choi, E., Thoutireddy, P., Gurnis, M., & Aivazis, M. (2006). GeoFramework: Coupling multiple models of mantle convection within a computational framework. *Geochemistry, Geophysics, Geosystems*, *7*(6), 1. https://doi.org/10.1029/2005GC001155

Tang, J., Xu, W., Wang, F., & Ge, W. (2018). Subduction history of the Paleo-Pacific slab beneath Eurasian continent: Mesozoic-Paleogene magmatic records in Northeast Asia. *Science China Earth Sciences*, *61*(5), 527–559. https://doi.org/10.1007/s11430-017-9174-1

Taramón, J. M., Rodríguez-González, J., Negredo, A. M., & Billen, M. I. (2015). Influence of cratonic lithosphere on the formation and evolution of flat slabs: Insights from 3-D time-dependent modeling. *Geochemistry, Geophysics, Geosystems*, *16*(9), 2933–2948. https://doi.org/10.1002/2015GC005940

Torsvik, T. H., Steinberger, B., Shephard, G. E., Doubrovine, P. V., Gaina, C., Domeier, M., et al. (2019). Pacific-Panthalassic reconstructions: Overview, errata and the way forward. *Geochemistry, Geophysics, Geosystems*, *20*(7), 3659–3689. https://doi.org/10.1029/2019GC008402

Trumbull, R. B., Riller, U., Oncken, O., Scheuber, E., Munier, K., & Hongn, F. (2006). The time-space distribution of Cenozoic volcanism in the South-Central Andes: A new data compilation and some tectonic implications. *Andes*, 29–43. https://doi.org/10.1007/978-3-540-48684-8_2

van Hunen, J., van den Berg, A. P., & Vlaar, N. J. (2000). A thermo-mechanical model of horizontal subduction below an overriding plate. *Earth and Planetary Science Letters*, *182*(2), 157–169. https://doi.org/10.1016/S0012-821X(00)00240-5

van Hunen, J., van den Berg, A. P., & Vlaar, N. J. (2002). On the role of subducting oceanic plateaus in the development of shallow flat subduction. *Tectonophysics*, *352*(3–4), 317–333. https://doi.org/10.1016/S0040-1951(02)00263-9

van Hunen, J., van den Berg, A. P., & Vlaar, N. J. (2004). Various mechanisms to induce present-day shallow flat subduction and implications for the younger Earth: A numerical parameter study. *Physics of the Earth and Planetary Interiors*, *146*(1–2), 179–194. https://doi.org/10.1016/j.pepi.2003.07.027

Wu, F. Y., Yang, J. H., Xu, Y. G., Wilde, S. A., & Walker, R. J. (2019). Destruction of the north China craton in the Mesozoic. *Annual Review of Earth and Planetary Sciences*, *47*, 173–195. https://doi.org/10.1146/annurev-earth-053018-060342

Xu, Y. G. (2001). Thermo-tectonic destruction of the Archaean lithospheric keel beneath the Sino-Korean Craton in China: Evidence, timing and mechanism. *Physics and Chemistry of the Earth—Part A: Solid Earth and Geodesy*, *26*(9–10), 747–757. https://doi.org/10.1016/S1464-1895(01)00124-7

Xu, Y. G. (2007). Diachronous lithospheric thinning of the North China Craton and formation of the Daxin'anling-Taihangshan gravity lineament. *Lithos*, *96*(1–2), 281–298. https://doi.org/10.1016/j.lithos.2006.09.013

Yang, T., & Gurnis, M. (2016). Dynamic topography, gravity and the role of lateral viscosity variations from inversion of global mantle flow. *Geophysical Journal International*, *207*(2), 1186–1202. https://doi.org/10.1093/gji/ggw335

Zhang, J. H., Gao, S., Ge, W. C., Wu, F. Y., Yang, J. H., Wilde, S. A., & Li, M. (2010). Geochronology of the Mesozoic volcanic rocks in the Great Xing'an Range, northeastern China: Implications for subduction-induced delamination. *Chemical Geology*, *276*(3–4), 144–165. https://doi.org/10.1016/j.chemgeo.2010.05.013

Zhang, N., & Li, Z. X. (2018). Formation of mantle "lone plumes" in the global downwelling zone—A multiscale modelling of subduction-controlled plume generation beneath the South China Sea. *Tectonophysics*, *723*, 1–13. https://doi.org/10.1016/j.tecto.2017.11.038

Zhang, R., Wu, Q., Sun, L., He, J., & Gao, Z. (2014). Crustal and lithospheric structure of Northeast China from S-wave receiver functions. *Earth and Planetary Science Letters*, *401*, 196–205. https://doi.org/10.1016/j.epsl.2014.06.017

Zhang, X., Chung, S.-L., Lai, Y.-M., Ghani, A. A., Murtadha, S., Lee, H.-Y., & Hsu, C.-C. (2019). A 6000-km-long Neo-Tethyan arc system with coherent magmatic flare-ups and lulls in South Asia. *Geology*, *47*(6), 573–576. https://doi.org/10.1130/G46172.1

Zhang, Y., Chen, L., Ai, Y., & Jiang, M. (2019). Lithospheric structure beneath the central and western North China Craton and adjacent regions from S-receiver function imaging. *Geophysical Journal International*, *219*(1), 619–632. https://doi.org/10.1093/gji/ggz322

Zhang, Y., Chen, L., Ai, Y., Jiang, M., Xu, W., & Shen, Z. (2018). Lithospheric structure of the South China Block from S-receiver function. *Chinese Journal of Geophysics*, *61*(1), 138–149. https://doi.org/10.6038/cjg2018L0226

Zhong, S., McNamara, A., Tan, E., Moresi, L., & Gurnis, M. (2008). A benchmark study on mantle convection in a 3-D spherical shell using CitcomS. *Geochemistry, Geophysics, Geosystems*, *9*(10), 1. https://doi.org/10.1029/2008GC002048

Zhou, Q., Hu, J., Liu, L., Chaparro, T., Stegman, D. R., & Faccenda, M. (2018). Western U.S. seismic anisotropy revealing complex mantle dynamics. *Earth and Planetary Science Letters*, *500*, 156–167. https://doi.org/10.1016/j.epsl.2018.08.015

Zhou, Q., & Liu, L. (2019). Topographic evolution of the western United States since the early Miocene. *Earth and Planetary Science Letters*, *514*, 1–12. https://doi.org/10.1016/j.epsl.2019.02.029

Zhou, Q., Liu, L., & Hu, J. (2018). Western US volcanism due to intruding oceanic mantle driven by ancient Farallon slabs. *Nature Geoscience*, *11*(1), 70–76. https://doi.org/10.1038/s41561-017-0035-y

Zhou, X. M., & Li, W. X. (2000). Origin of late Mesozoic igneous rocks in Southeastern China: Implications for lithosphere subduction and underplating of mafic magmas. *Tectonophysics*, *326*(3–4), 269–287. https://doi.org/10.1016/S0040-1951(00)00120-7